

# Searching for supermassive black hole binaries within SRG/eROSITA-De

## I. Properties of the X-ray selected candidates

Dusán Tubín-Arenas<sup>1,2,\*</sup>, Mirko Krumpe<sup>1</sup>, David Homan<sup>1</sup>, Alex Markowitz<sup>3</sup>, Meredith Powell<sup>1</sup>, Georg Lamer<sup>1</sup>, Tanya Urrutia<sup>1</sup>, Axel Schwope<sup>1</sup>, Hartmut Winkler<sup>5</sup>, Sabina Bahic<sup>1,2</sup>, Johannes Buchner<sup>4</sup>, Carolina Andonie<sup>4</sup>, Mara Salvato<sup>4</sup>, Andrea Merloni<sup>4</sup>, Jan Kurpas<sup>1,2</sup>, Stefano Ciroi<sup>6</sup>, Francesco di Mille<sup>7</sup>, Avinash Chaturvedi<sup>1</sup>, Arne Rau<sup>4</sup>, Zsófi Igo<sup>4</sup>, Iuliia Grotova<sup>4</sup>, Zhu Liu<sup>8,4</sup>, and Kirpal Nandra<sup>4</sup>

<sup>1</sup> Leibniz-Institut für Astrophysik Potsdam (AIP), An der Sternwarte 16, 14482 Potsdam, Germany

<sup>2</sup> Potsdam University, Institute for Physics and Astronomy, Karl-Liebknecht-Straße 24/25, 14476 Potsdam, Germany

<sup>3</sup> Nicolaus Copernicus Astronomical Center, Polish Academy of Sciences, ul. Bartycka 18, 00-716 Warszawa, Poland

<sup>4</sup> Max-Planck-Institut für extraterrestrische Physik, Gießenbachstraße 1, 85748 Garching, Germany

<sup>5</sup> Dept. Physics, University of Johannesburg, PO Box 524, 2006 Auckland Park, Johannesburg, South Africa

<sup>6</sup> Department of Physics and Astronomy, University of Padova, Via F. Marzolo 8, I-35131 Padova, Italy

<sup>7</sup> Las Campanas Observatory – Carnegie Institution for Science, Colina el Pino, Casilla 601, La Serena, Chile

<sup>8</sup> Centre for Astrophysics Research, University of Hertfordshire, College Lane, Hatfield AL10 9AB, UK

Received 25 March 2025 / Accepted 29 April 2025

## ABSTRACT

**Context.** Supermassive black hole binaries (SMBHBs) with separations on (sub)pc scales represent one of the latest stages of hierarchical galaxy assembly. However, many of these objects are hidden behind large columns of gas and dust at the centers of galaxies and are difficult to detect. In these systems, accretion is expected to take the form of two individual accretion disks around the individual black holes, fed by a larger circumbinary disk. The X-ray and UV emission in these systems are predicted to vary regularly on timescales that are comparable to that of the orbital period of the binary.

**Aims.** This is the first of a series of papers where we continue to search for and characterize SMBHB candidates based on quasiperiodic light curves from the soft X-ray instrument eROSITA on board the Spectrum-Roentgen-Gamma (SRG) observatory and extensive X-ray follow-up.

**Methods.** We searched the multi-epoch *SRG/eROSITA* all-sky surveys for extragalactic sources that show an “up-down-up-down” or “down-up-down-up” profile (from scan to scan) in their 0.2–2.3 keV flux light curves. We selected sources where the “up” and “down” flux levels vary by at least  $3\sigma$ . The “down” states were also allowed to correspond to nondetections. We excluded stellar objects, blazars, and radio-loud active galactic nuclei (AGNs) via Gaia DR3 parallaxes and proper motions. We also carried out a visual inspection of the images drawn from the Legacy Survey DR10 and the SIMBAD database.

**Results.** We compiled a sample of 16 sources that are suitable for X-ray follow-up campaigns given their brightness and significant variability between bright and faint *SRG/eROSITA* flux levels. We triggered extensive *Swift*-XRT and *NICER* monitoring campaigns on the best SMBHB candidates to confirm or discard their tentative periodicities. Optical spectroscopic observations confirmed the nuclear and extragalactic nature of 15/16 objects and enabled single-epoch SMBH mass measurements and BPT classifications of the dominant ionization in the host galaxy. Our most promising candidate, eRASS<sup>1</sup> J0530-4125, exhibits X-ray quasi-periodic variability with a typical time scale of one year in the observed frame. By stacking the X-ray observations of each source in our sample, we found that 14 out of the 15 sources can be modeled by a power law with a photon index ranging from  $\Gamma \sim 1.8$ –2.8. Based on our selection, we estimate an optimistic upper limit on the fraction of SMBHB candidates to be  $\sim 0.05$  per galaxy. We emphasize that further observational evidence is needed to confirm the SMBHB nature of our sources.

**Key words.** galaxies: active – galaxies: nuclei – quasars: supermassive black holes – X-rays: galaxies

## 1. Introduction

The formation of supermassive black hole (SMBH) binaries is thought to be a direct consequence of the  $\Lambda$ CDM cosmological framework, whereby galaxies hierarchically grow through frequent mergers (see e.g., [White & Rees 1978](#); [White & Frenk 1991](#)). In this scenario, there is a clear link between large-scale structure formation and gravitational wave physics.

During a major galaxy merger event, two (or more) SMBHs may be active and embedded in the merging system, separated on kiloparsec scales. This is the so-called dual active galactic nuclei (AGN) phase. Detailed studies of dual AGNs reveal a vast set of astrophysical processes between the active SMBHs and the host galaxies, such as high-velocity outflows ([Treister et al. 2018](#)), extended AGN ionization in the host galaxy ([Tubín et al. 2021](#)), or even triple SMBH systems ([Kollatschny et al. 2020](#)). Statistically, the dual AGN fraction, luminosity, and obscuration

\* Corresponding author: dtubin@aip.de

all increase with decreasing AGN separation (see e.g., Koss et al. 2012, 2018; Ricci et al. 2017; De Rosa et al. 2023).

Over the course of the merger, dynamical friction (Chandrasekhar 1943) will efficiently remove angular momentum from the SMBH orbits and form an inspiraling binary system at parsec (pc) separations (Begelman et al. 1980). At these spatial scales, the SMBHs become gravitationally bound in a SMBH binary (SMBHB). The projected distances between the SMBHB are small and are virtually impossible to resolve for most of the telescope facilities, especially for nonlocal galaxies.

Since the dynamical friction becomes inefficient due to the low stellar density at pc-scales, the SMBHB can potentially remain in orbit for a period that is several times longer than the Hubble time. This is known as the “final parsec” problem (Milosavljević & Merritt 2003), which highlights the need for external effects to bring the SMBHs to millipc scales. Nonspherical stellar potentials of galaxies (see e.g., Vasiliev et al. 2014; Mirza et al. 2017), injection of gas into the system (Escala et al. 2005; Lodato et al. 2009), or scattering with stars and massive black holes (see e.g., Ryu et al. 2018) are all processes that could remove angular momentum from the binary.

The recent detection of the gravitational-wave background (GWB) using pulsar timing arrays (PTA; EPTA Collaboration 2023; Reardon et al. 2023; Xu et al. 2023) suggests the presence of a population of massive binaries (with masses ranging between  $10^8$ – $10^{10} M_\odot$ ) that are close enough (0.001–0.01 pc separation) to produce gravitational waves in nanohertz frequencies across the universe (Agazie et al. 2023; EPTA Collaboration 2024). The GWB results and the expected population of SMBHBs suggest that there is a mechanism that removes angular momentum from these SMBHBs. This brings them closer until gravitational wave production efficiently removes angular momentum from the binary, eventually leading to mergers on timescales shorter than the Hubble time.

However, the biggest challenge in confirming the existence of SMBHBs and characterizing their demographics is detecting the electromagnetic counterparts of SMBHBs. These objects are usually separated by (sub)pc scales to be spatially resolved by current facilities and likely obscured at the centers of galaxies. A well-characterized population of SMBHBs could constrain the physics and timescales associated with the gravitationally bounded SMBHBs.

The presence of gas surrounding the binary provides a way to detect SMBHBs and their electromagnetic features. Hydrodynamic simulations predict that each SMBH at sub-pc separation accretes material from a circumbinary disk (Noble et al. 2012; Farris et al. 2014, 2015) via accretion inflows, forming smaller and independent mini-accretion disks around each SMBHs (Hayasaki et al. 2008; d’Ascoli et al. 2018; Bowen et al. 2018). The presence of the two SMBHs will create cavities in the circumbinary disk (D’Orazio et al. 2013), creating a deficit of optical-UV radiation compared to single-SMBH accretion disks (see, e.g., Gültekin & Miller 2012; Roedig et al. 2014; Wang et al. 2023). Furthermore, X-ray and hard UV emission are expected to originate mainly from the inner mini-disks around each SMBH (Sesana et al. 2012; d’Ascoli et al. 2018), while optical and infrared emission come from the circumbinary disk (see e.g., Tanaka et al. 2012).

Comprehensive reviews on the search and observational evidence of SMBHBs have been reported by De Rosa et al. (2019), Bogdanović et al. (2022), and D’Orazio & Charisi (2023). In addition, D’Orazio & Charisi (2023) recently compiled a complete summary of the multiwavelength observational efforts to search for SMBHBs and the known SMBHB candidates. In the

following, we describe the most relevant multiwavelength and multitechnique efforts to search for SMBHBs.

Extragalactic sources with periodic light curves have long been discussed and used as a first step to identifying close SMBHB candidates. X-ray and UV light curves are expected to vary regularly with periods comparable to that of the binary period (Bowen et al. 2018, 2019; Tang et al. 2018; Kelley et al. 2019; Westernacher-Schneider et al. 2022) since the minidisks are periodically fed by gas inflow from the circumbinary disk (Hayasaki et al. 2008; Farris et al. 2014). Doppler beaming (D’Orazio et al. 2015; Charisi et al. 2018) or gravitational lensing (Haiman 2017; D’Orazio & Di Stefano 2018) can also produce periodical features in the light curves of SMBHBs. Further evidence for the binary scenario comes from detections of double peaks or ripples in the Fe  $K\alpha$  emission line profile in the X-rays (see, e.g., Sesana et al. 2012; McKernan et al. 2013; McKernan & Ford 2015; Jovanović et al. 2020).

However, the periodic behavior observed in X-ray light curves can have several causes. One of the most common producers of spurious periodicities is the “normal” AGN variability. Accretion onto single SMBHBs produces highly variable X-ray emission with a stochastic behavior (known as red noise; see, e.g., Press 1978; Vaughan et al. 2003). This stochastic behavior can mimic both strictly periodic and quasiperiodic variability for a few cycles (Krishnan et al. 2021; Witt et al. 2022). This implies that tests for periodicities can easily yield false positives (Press 1978; Krishnan et al. 2021), even if no periodic signals are inherently present in the data. In the presence of real periodicity, deconvolving the red noise and the periodic signal is difficult and can be hampered by the quality and cadence of the data.

Regular monitoring campaigns spanning several years at high energies are only available in exceptional cases. For example, Serafinelli et al. (2020) and Liu et al. (2020) carried out independent systematic searches for periodic variable AGN in hard X-ray (14–195 keV) sources within the 105-month *Swift*-BAT survey. Serafinelli et al. (2020) found two SMBHB candidates with tentative periodicities, namely, MCG+11-11-032 and Mrk 915. On the other hand, Liu et al. (2020) did not find any evidence of periodic AGNs in a slightly larger *Swift*-BAT sample that includes the previous two sources.

MCG+11-11-032 is a SMBHB candidate that was initially selected as a dual AGN candidate based on its double-peaked optical emission lines. Its X-ray emission hints at a period of 26 months with a double-peaked Fe  $K\alpha$  line (shifted by  $\Delta E = 0.4 \pm 0.2$  keV) that has been claimed at a  $4\sigma$  confidence (Severgnini et al. 2018). Mrk 915, on the other hand, does not show a double-peaked Fe  $K\alpha$  line, but it does have a tentative X-ray periodicity of 35 months (Serafinelli et al. 2020). In these objects, the distances between the SMBHBs would be 5 and 6.5 milli-pc, respectively. Another claimed SMBHB candidate is OJ 287 (Sillanpää et al. 1988; Dey et al. 2019a). Extensive multiwavelength monitoring observations, including *Swift*-XRT campaigns, have been implemented on OJ 287 to claim the presence of an eccentric secondary SMBH orbit with a mass ratio of  $q \simeq 0.01$  that crosses the accretion disk of the main SMBH twice every  $\sim$ 12 years (see e.g., Komossa et al. 2021a,b, for the project Multiwavelength Observations and Modeling, MOMO, of OJ 287).

Periodicities in other wavelengths have also been proposed as tracers of SMBHBs. Optical photometric variability studies performed on survey data provide a vast initial sample of  $\sim$ 150 periodic SMBHB candidates (see e.g., Graham et al. 2015;

Charisi et al. 2016; Liu et al. 2016a). Most of these candidates are on timescales that place them in a regime where the robust separation of red noise from periodicities is difficult, as stochastic accretion effects can lead to spurious signals given a limited observation duration or gappy data sampling (Vaughan et al. 2016; Liu et al. 2018; Krishnan et al. 2021). Recently, Luo et al. (2025) conducted the first systematic search for SMBHB candidates with periodic light curves from Wide-field Infrared Survey Explorer (WISE) infrared (IR) data. However, their mock simulation of the parent sample indicates that stochastic variability can produce a similar number of periodic sources. Periodicity observed in radio-loud sources has been attributed to the presence of a SMBHB in the center of the galaxy; however, this could also be due to other single AGN processes (Holgado et al. 2018) such as jet precession (Caproni et al. 2013; Liska et al. 2018) or the intrinsic variability of the accretion flow in the accretion disc (King et al. 2013). The presence of SMBHBs have also been invoked to explain periodicities of a few cycles that have been found in radio data of individual blazars (see e.g., Ren et al. 2021; O’Neill et al. 2022; Kiehlmann et al. 2024; de la Parra et al. 2024).

Spectroscopic features like line asymmetries, double-peaks, velocity shifts, or line profile variability on broad emission lines such as H $\beta$  or H $\alpha$  have been proposed as evidence of orbital motion and a consequence of a black hole binary in the center of AGNs (Tsalmantza et al. 2011; Eracleous et al. 2012; Shen et al. 2013; Liu et al. 2014; Runnoe et al. 2017; Doan et al. 2020; Jovanović et al. 2025). One example of this is the Seyfert galaxy NGC 4151. Radial velocity curves show flux variations in the H $\alpha$  light curve that suggest an orbital motion that is consistent with the signature of a sub-pc SMBHB system with an orbital period of about  $\sim$ 5700 days (Bon et al. 2012). However, in some sources, radial-velocity shifts of the broad-line components are found to be inconsistent with the expected orbital motion of a SMBHB (Wang et al. 2017). Eracleous et al. (2009) and Liu et al. (2016b) find evidence that double-peaked line profiles can also be produced by single (nonbinary) AGN broad line regions (BLR). Detailed modeling and extensive time-resolved spectroscopic studies are still needed to understand the spectral features expected for SMBHBs (see e.g., Popović 2012; De Rosa et al. 2019, for a detailed discussion on the hypothesis and challenges using broad emission lines as tracers of SMBHBs).

Periodic X-ray emission seems to be one of the most promising ways to identify SMBHB candidates. The X-ray photons can penetrate the obscuring gas and dust, and in SMBHBs are mainly emitted in regions very close to the orbiting SMBHBs. Therefore, the X-ray emission is expected to vary regularly with periods comparable to that of the binary period (e.g., Hayasaki et al. 2007; MacFadyen & Milosavljević 2008; D’Orazio et al. 2013; Farris et al. 2014). However, the X-ray coverage of the sky and the regular monitoring of X-ray sources have been limited. The launch of the extended ROentgen Survey with an Imaging Telescope Array (eROSITA; Merloni et al. 2012; Predehl et al. 2021) has opened a window to the search and discovery of peculiar AGNs in one of the largest and most sensitive X-ray catalogs to date. eROSITA is the soft X-ray instrument on board the *Spectrum-Roentgen-Gamma* (SRG; Sunyaev et al. 2021) observatory and provides an unprecedented opportunity for regular, all-sky X-ray monitoring thanks to its scanning strategy. Therefore, eROSITA enables extensive time-domain studies of the X-ray sky. The survey has already been used to compile a catalog of highly variable extragalactic transients between the first and second eROSITA sky scans (Grotova et al. 2025).

This work is the first in a series of papers that aim to find and confirm SMBHBs based on data from one of the largest X-ray all-sky catalogs ever obtained. Here, we exploit the SRG/eROSITA all-sky data to identify extragalactic objects that show quasiperiodic X-ray light curves as a first attempt to compile a list of SMBHB candidates. We obtained additional extensive X-ray follow-up, optical spectra, and complementary multiwavelength data to constrain the nature of the selected sources. According to the current theories, a confirmation of the SMBHB scenario is based on the detection of (i) persistent quasiperiodic X-ray signatures for multiple periods and (ii) the confirmation of double-peaked Fe K $\alpha$  lines that shift in energy with the orbital period of the SMBHB. We note that there is other interesting proposed evidence for SMBHB, such as the periodic ripples in the line profile, which consist of a pair of dips in the broad line blueward and redward from the line centroid energy (see e.g., Jovanović et al. 2014, 2020; McKernan & Ford 2015). However, high-signal-to-noise X-ray observations are needed to observe these features (see e.g., McKernan & Ford 2015). Since our selection is mainly based on quasiperiodic behavior that can also be produced by stochastic accretion, a detailed assessment of the red noise in our sample selection will be made in the second paper of the series (Tubín-Arenas et al., in prep.). Upcoming papers will also present longer and deeper X-ray follow-up data obtained after the time of writing this paper.

The paper is structured as follows. In Sect. 2, we describe the SRG/eROSITA scanning pattern and how we searched for quasiperiodic signals within the eROSITA data. In Sect. 3, we present the additional infrared, optical, UV, and X-ray data for the selected objects. Since we have continuously monitored the sources in X-rays, this paper is based on all X-ray data obtained until December 31, 2024. In Sect. 4, we analyze the multiwavelength data from follow-up observations. In Sect. 5, we present the optical and X-ray properties of the selected sample, including a detailed discussion of the two most well-monitored SMBHB candidates. We discuss the nature of the variability from different physical perspectives and constrain their abundances in Sect. 6. Finally, we present our conclusions in Sect. 7. Throughout this paper, we assume a  $\Lambda$ CDM cosmology with  $h_0 = 0.7$ ,  $\Omega_m = 0.27$  and  $\Omega_\Lambda = 0.73$  (Hinshaw et al. 2009). Unless explicitly stated otherwise, we report all errors corresponding to 68% confidence ( $1\sigma$ ) intervals.

## 2. SRG/eROSITA and the SMBHB quest

### 2.1. Overview of eROSITA all-sky scans

SRG/eROSITA combines a large field of view (FoV  $\sim 1^\circ$ ), an effective scanning observation mode, and high sensitivity in the soft X-ray band (0.2–2.3 keV), making it the most efficient imaging survey telescope in X-rays (Merloni et al. 2012; Predehl et al. 2021). By February 2022, SRG/eROSITA completed four and one-third of the planned eight eROSITA all-sky scans (eRASS; Predehl et al. 2021). SRG/eROSITA executes one all-sky scan by rotating around the observing axis (which is perpendicular to the axis that connects the spacecraft with the Sun) every 4 hours (referred to as one “eROday”) and shifting its orbit by one degree per day, covering the whole sky in approximately 182 days (half a year). Each position close to the ecliptic equator is observed typically six times for up to 40 seconds per eROday, while sources close to the ecliptic poles are observed more often, creating regions of deep exposure (see Fig. 3 in Merloni et al. 2024).

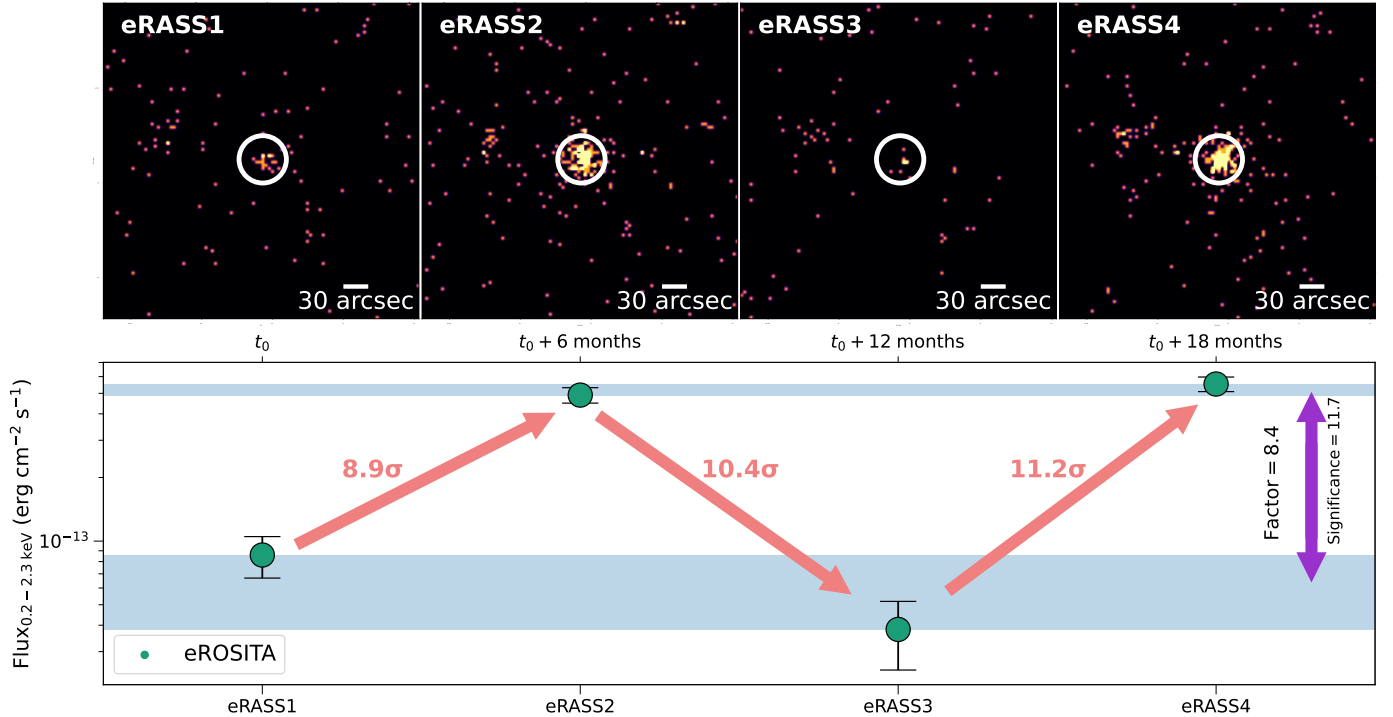


**Fig. 1.** Visualization of the selection for SMBHB candidates based on their *SRG/eROSITA* light curves. Top panel: Observed counts at the position of the source eRASS1 J0530-4125 (see Table 1) at every *SRG/eROSITA* scan in the 0.2–2.3 keV energy band. Each image is temporally spaced every six months. The white circles correspond to a typical aperture with a radius of 30'', similar to the scale bar displayed on the bottom right side of each panel. Lower panel: X-ray light curve of eRASS1 J0530-4125. The colored arrows indicate the significance of the flux change between the consecutive scans. The blue-shaded areas indicate the bright and faint flux levels of the source, while the purple arrow shows the factor and significance between these two flux levels.

Following this strategy, eROSITA detected  $\sim 1$  million sources during the first all-sky survey on the Western Galactic hemisphere (eROSITA-De: with Galactic longitudes between  $180 \lesssim l \lesssim 360$ , Merloni et al. 2024). For nondetected, variable, or transient sources that fall below the detection threshold of the eSASS pipeline, Tubín-Arenas et al. (2024) provide *SRG/eROSITA* upper flux limits based on X-ray aperture photometry on the eROSITA standard calibration data products (counts image, background image, and exposure time). These detected fluxes and upper limits are used in the search for periodically variable SMBHB candidates.

## 2.2. Sample selection

### 2.2.1. eROSITA light curve selection

When the four completed all-sky scans are stacked, the sensitivity increases, resulting in approximately three million detected sources. The eRASS:4 catalog (stacked version of the eRASS1 to eRASS4 catalogs – an internal eROSITA-De consortium product, version 230427) is the deepest, most sensitive, and most complete all-sky X-ray catalog available at 0.2–2.3 keV. It also provides relevant information such as positions, observation dates, and fluxes for each independent eRASS survey used in the stacking process. Therefore, the eRASS:4 catalog delivers immediate eROSITA X-ray light curves.

We set out to explore this eROSITA stacked catalog with epoch information to search for quasiperiodic signals. Since eROSITA observed the sky every six months for almost two and a half years, we are sensitive to quasiperiods of about one year, as well as shorter period harmonics (e.g., four months). Therefore, we have searched for sources that show an “up-down-up-

down” or “down-up-down-up” profile in their eROSITA light curve. The top panel of Fig. 1 shows an example of an extragalactic source that follows such a flux pattern. Our eROSITA source selection was based on three criteria, described below.

First, we request that the consecutive “up” and “down” flux measurements to differ by  $>3\sigma$  for an object to be preliminary included in our initial sample of candidates. Thus, we have

$$\frac{F_i - F_{i+1}}{\sqrt{F_{i,\text{err}}^2 + F_{i+1,\text{err}}^2}} > 3,$$

where  $i = 1, 2, 3, 4$  is the corresponding eRASS scan, then  $F_i$  and  $F_{i,\text{err}}$  are the flux and flux error for the eRASS scan,  $i$ , of a given source. In the case where the source falls into the sky region where we have five eROSITA scans, we require the above-mentioned criterion for eRASS1 to eRASS5 ( $i = 1, 2, 3, 4, 5$ ). Figure 1 illustrates this selection criterion as the source varies by almost  $10\sigma$  between the flux measurements spaced apart by six months. The “down” states are also allowed to be nondetections. In these cases, we use the corresponding  $3\sigma$  eROSITA upper flux limit values in the 0.2–2.3 keV band (Tubín-Arenas et al. 2024).

For the next two selection criteria, we first defined “bright” and “faint” states based on the average flux of all the “up” data points and the average flux of all the “down” data points for each source. The uncertainty ranges of the bright and faint states ( $F_{\text{bright},\text{err}}$ ,  $F_{\text{faint},\text{err}}$ , respectively) are given by the standard deviation of the individual fluxes contributing to the corresponding level and are represented by the blue-shaded areas in the bottom panel of Fig. 1. These uncertainties also give us an idea of how consistent the flux measurements are in either of the two flux states.

Next, we compute a factor,  $F$ , that corresponds to the ratio between the average fluxes of the bright and the low flux levels for every source ( $F = F_{\text{bright}}/F_{\text{faint}}$ ). Only sources with  $F > 3$  are thus selected.

Finally, we calculate the significance as

$$S = \frac{F_{\text{bright}} - F_{\text{faint}}}{\sqrt{F_{\text{bright,err}}^2 + F_{\text{faint,err}}^2}}.$$

This is the flux difference normalized by the error between the bright and faint flux levels for every source. Here, we require a value of at least  $S = 3$ .

### 2.2.2. Excluding galactic sources

As a first attempt to remove a significant fraction of stellar sources from our light curve selection, we used the proper motion and parallax values from *Gaia* DR3 (Gaia Collaboration 2021). We cross-matched our eROSITA sources to *Gaia* sources using a 15-arcsecond matching radius. If multiple *Gaia* sources were found for one eROSITA source, we considered the closest *Gaia* source as the likely counterpart. Since we later visually inspected the remaining candidates, we emphasize that this matching procedure only helps to reduce the workload of the visual screening.

We excluded stellar sources by requesting our sources to have a parallax and proper motion (RA and Dec combined) significance consistent with zero within  $3\sigma$  and  $5\sigma$ , respectively. Sources without *Gaia* counterparts were kept in our sample, as it is unclear whether they are faint, distant stellar objects or of extragalactic origin.

As a next step, we visually inspected the Legacy Survey Data Release 10 (LS DR10; Dey et al. 2019b) images of the remaining sources. For objects not covered in LS DR10, we inspected the Digitized Sky Survey (DSS; Lasker et al. 1996) images. For a few sources, bright saturated stars were identified as their counterparts. We rejected these objects from our candidate sample. We also checked the SIMBAD database (Wenger et al. 2000) for the remaining objects. If a stellar object was listed within 15 arcseconds of our X-ray position, we also excluded these objects from our candidate sample. The SIMBAD database was also used to identify known blazars and radio-loud AGNs. The latter category was removed as well since jet precession could also produce periodic X-ray emission (Liska et al. 2018). As a result of these steps, we are confident that our sample contains little to no contamination from galactic objects.

### 2.2.3. Primary SMBHB candidate sample

The candidate sample consists of 119 extragalactic objects. Figure 2 shows the distribution of their factors  $F$  and significances  $S$ . All objects shown fulfill our selection criteria of at least  $3\sigma$  difference in X-ray flux between each adjacent epoch,  $F > 3$ , and a significance of at least  $S > 3$ .

Extended light-curve information for all sources is needed to confirm or rule out each quasiperiodic light curve signature. However, this would require a massive X-ray follow-up campaign. Therefore, we decided to focus our X-ray follow-up resources on the brightest and most variable objects. The objects must have a  $F > 5$ , an X-ray flux in the bright state  $F_{\text{bright}} \gtrsim 5 \times 10^{-13} \text{ erg s}^{-1} \text{ cm}^{-2}$  to allow a follow-up program with missions like *Swift* and *NICER*, or have already publicly available follow-up data. This then defines our primary SMBHB

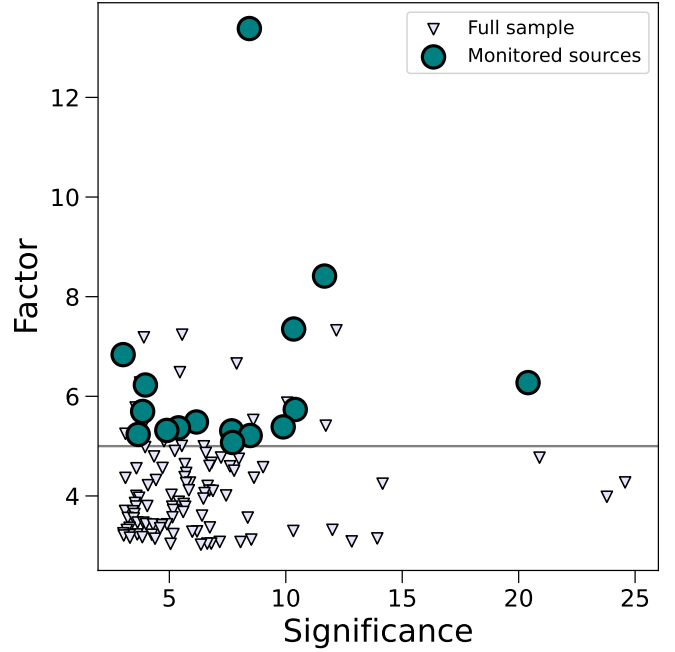


**Fig. 2.** Distribution of the sample based on the factor ( $F = F_{\text{bright}}/F_{\text{faint}}$ ) and significance ( $S = \frac{F_{\text{bright}} - F_{\text{faint}}}{\sqrt{F_{\text{bright,err}}^2 + F_{\text{faint,err}}^2}}$ ) values (see Sect. 2.2). For each source, the factor and significance are calculated between the bright and faint states represented by the blue-shaded area in Fig. 1. We make a cut at  $F > 5$  and highlight the 16 sources that will be the focus of this paper. The remaining extragalactic sources of the sample are displayed with triangles.

candidate sample of 16 sources highlighted in Fig. 2. A summary of their properties is given in Table 1.

## 3. Data and data reduction

Our X-ray monitoring programs were aimed at observing the candidates once every month for five months (six pointings in total) to fill in the eROSITA gaps and increase the observing cadence. We began monitoring in the month that eROSITA would have observed the source again if the survey had continued after February 2022. Therefore, assuming that the pattern of the eROSITA light curve continues over time, we can study the X-ray variability and emission properties of the candidates in more detail. We used these follow-up observations to discriminate between tentative quasiperiodic signals and red-noise-driven variability. Sources displaying tentative periodicities after an initial one-month cadence follow-up were eligible for X-ray monitoring programs with a higher cadence.

In addition to the X-ray follow-up, we obtained multiwavelength imaging, photometry, and spectroscopic data for the final SMBHB candidate sample. Optical spectra were obtained for known and previously unclassified objects to confirm their extragalactic nature. Here, we describe the multiwavelength data used in this paper.

### 3.1. Infrared data

Mid-infrared (mid-IR) photometry data was collected from the NEOWISE-R mission (Wright et al. 2010; Mainzer et al. 2014) in the W1 and W2 bands, centered at 3.4 and 4.6 microns, respectively. The data were retrieved via the unTimely catalog

**Table 1.** Primary SMBHB candidates catalog.

Name	RA(2000) ( $^{\circ}$ )	Dec(2000) ( $^{\circ}$ )	Radec_err (68%)	Separation ( $\Delta''$ )	Sig.	Factor	Detection Likelihood	X-ray follow-up
1 – eRASSt J0344-3327	56.107460	-33.45521	1.09	0.17	8.4	13.4	473.7	<i>Swift</i> -XRT, <i>NICER</i>
2 – eRASSt J0530-4125	82.56909	-41.42582	0.84	1.87	11.7	8.4	1106.2	<i>Swift</i> -XRT, <i>NICER</i>
3 – eRASSt J1906-4850	286.53654	-48.84064	0.49	1.02	10.3	7.4	3788.3	<i>Swift</i> -XRT, <i>NICER</i>
4 – eRASSt J0432-3023	68.07197	-30.39961	0.63	1.23	3.0	6.8	1837.3	<i>Swift</i> -XRT, <i>NICER</i>
5 – eRASSt J1130-0806	172.61730	-8.10278	1.18	2.33	20.4	6.3	420.9	–
6 – eRASSt J1522-3722	230.56415	-37.37989	0.85	1.24	4.0	6.2	732.1	<i>NICER</i>
7 – eRASSt J1141+0635	175.47668	6.58614	0.94	1.07	10.4	5.7	774.8	<i>Swift</i> -XRT, <i>NICER</i> , <i>XMM</i>
8 – eRASSt J0458-2159	74.66770	-21.99204	0.34	0.98	3.9	5.7	8437.1	<i>NICER</i>
9 – eRASSt J2227-4333	336.98212	-43.56079	1.42	1.35	6.2	5.5	271.5	–
10 – eRASSt J1124-0348	171.23409	-3.81142	1.17	0.93	9.9	5.4	509.8	<i>NICER</i>
11 – eRASSt J0036-3125	9.05142	-31.41707	1.26	1.30	5.4	5.4	413.2	–
12 – eRASSt J1003-2607	150.82466	-26.12018	1.08	1.62	4.9	5.3	709.1	<i>Swift</i> -XRT, <i>NICER</i>
13 – eRASSt J0818-2252	124.74048	-22.87709	0.52	1.36	7.7	5.3	5886.2	<i>Swift</i> -XRT, <i>NICER</i>
14 – eRASSt J0600-2939	90.23452	-29.65689	1.08	2.88	3.7	5.2	580.3	–
15 – eRASSt J0044-3313	11.20658	-33.23234	1.11	0.60	8.5	5.2	691.3	<i>Swift</i> -XRT
16 – eRASSt J0614-3835	93.71599	-38.59458	0.73	1.33	7.7	5.0	1450.6	–

**Notes.** Table with the eROSITA names of the sources (Column 1) and X-ray positions based on the stacked eRASS:4 coordinates (Columns 2 and 3). The “Radec\_err” values (Column 4) correspond to the combined positional  $1\sigma$  68% error derived from the PSF-fitting performed by the eROSITA source detection pipeline. The separation (Column 5) indicates the distance, in arcseconds, between the eROSITA and *Gaia* DR3 positions. We include the Significance (Column 6) and Factor (Column 7) parameters used in our SMBHB selection described in Sect. 2.2. We also show the detection likelihood (Column 8) from the eRASS:4 catalog, which corresponds to the negative log-likelihood probability that the source counts are produced by background fluctuations. Larger detection likelihoods correspond to more observed counts relative to the background and, therefore, a smaller likelihood that the observed counts were produced by background fluctuations. Finally, we also report the X-ray missions used to monitor the flux evolution of the candidates (Column 9). Five sources have not been observed. However, they will be targeted by *NICER* during cycle 7. The candidates are ranked according to their factor  $F$  values.

(Meisner et al. 2023) that are binned by  $\sim 180$  days to match the scanning pattern of the satellite. The infrared light curves are presented in Appendix A.

### 3.2. Optical

#### 3.2.1. Optical images

Figure 3 shows the optical images of the primary SMBHB candidates retrieved from the Legacy Survey Viewer<sup>1</sup> (Dey et al. 2019b). We mark the *SRG*/eROSITA X-ray position of the candidates, listed in Table 1, and the position of the optical counterpart detected by *Gaia*. All X-ray positions are consistent with their optical counterpart positions, considering  $3\sigma$  eROSITA positional uncertainties. This gives strong support to the idea that the X-ray emission is likely coming from the nuclear regions of the galaxy.

#### 3.2.2. Spectroscopic data

Optical spectroscopic observations were collected from the archive or newly obtained if missing. We aimed to confirm the extragalactic nature of our candidates, obtain redshifts, and thus study the intrinsic AGN properties of our sources, such as luminosity and SMBH mass. Column 2 of Table 2 lists the facilities used to obtain the optical spectroscopic observations of our SMBHB candidates. Four systems were observed with the ESO/La Silla EFOSC2 on the 3.6 m New Technology Telescope (NTT; program ID: 112.263K). The spectroscopic observations were performed with grating #13 and a 1'' slit width, which corresponds to a wavelength resolution of 15.5 Å in the range 3650–9250 Å. The ESO observations were reduced with the dedicated

software ESOReflex (version 2.11.5, Freudling et al. 2013) to correct for the standard bias, flats, wavelength, and flux calibration.

Eight candidates are bright and could, therefore, be observed with the SpUpNIC spectrograph (Crause et al. 2019) at the South African Astronomical Observatory (SAAO) 1.9 m telescope. The SAAO/SpUpNIC spectra were obtained with a 2.7'' slit width, a typical exposure time of two consecutive 1200 seconds, and a low-resolution grating to cover the entire optical range between  $\sim 3500$  Å and  $\sim 9000$  Å. The data were reduced using standard bias corrections and flat-fielding. The wavelength and spectrophotometric calibrations were performed using an Argon arc-lamp and a standard star spectra taken on the same night of observations.

Two spectra were taken with the IMACS Short-Camera (Dressler et al. 2011) mounted on the 6.5 m Baade Magellan telescope located at Las Campanas Observatory. The Magellan/Baade observations were carried out using a 1'' and 0''.7 slit with total exposures of 600 and 1080 seconds for eRASSt J1906-4850 and eRASSt J0458-2159, respectively. The spectra were reduced with IRAF (Tody 1986) following the usual procedure of overscan subtraction, flat-field correction, wavelength calibration using a He-Ne-Ar lamp, and a spectrophotometric standard star.

One optical spectrum (eRASSt J2227-4333) was retrieved from the archive of the 6dF Galaxy Survey (Jones et al. 2004, 2009).

Given its faint nature, we observed eRASSt J1003-2607 with the 8-meter class Large Binocular Telescope (LBT) using long-slit spectroscopy with the MODS spectrograph (Pogge et al. 2010). The observation was carried out on January 2nd, 2025, in one exposure of 3000 s with both the red and blue arms. The basic data reduction was done with the *modscCDRed* package<sup>2</sup>.

<sup>1</sup> <https://www.legacysurvey.org/viewer>

<sup>2</sup> <https://github.com/rwpogge/modscCDRed>

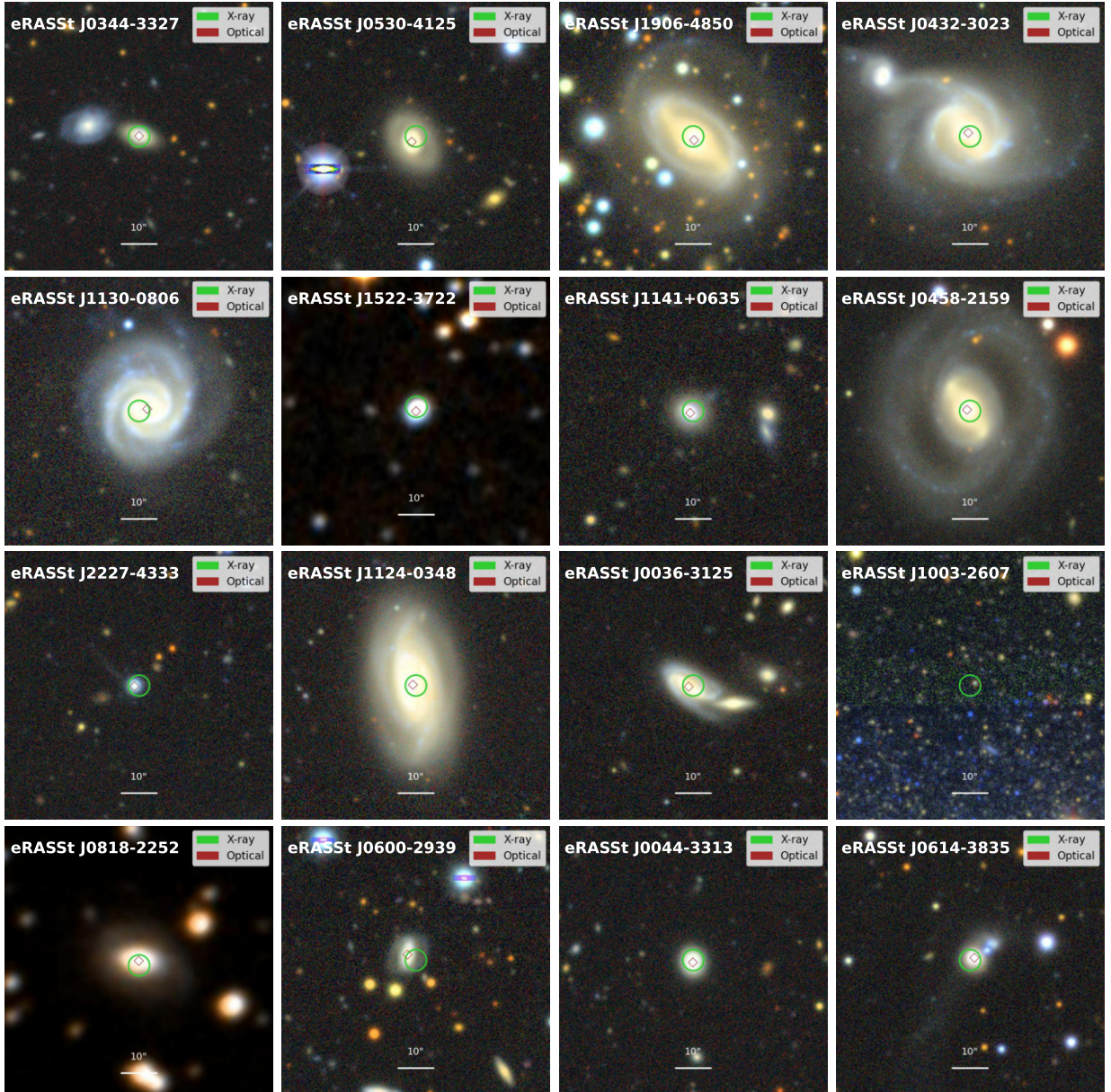


**Fig. 3.** Optical images of the SMBHB candidates. The cutout images were retrieved from the Legacy Survey Viewer with a pixel scale of 0.15 arcseconds per pixel and are centered at the *SRG/eROSITA* X-ray position of the candidates. We highlight the X-ray position with a green circle with a radius of  $3''$  that corresponds to a typical  $3\sigma$  positional uncertainty and the optical *Gaia* DR3 positions with a red diamond when available. Two sources (eRASSt J1522-3722 and eRASSt J0818-2252) are outside the LS footprint, therefore, we show the DSS images. eRASSt J1003-2607 was not detected by *Gaia* DR3 since the tentative source position highlighted inside the green circle is a faint source with a LS DR10 magnitude of  $m_r \sim 22$ . A  $10''$  scale bar is also shown at the bottom of the images for reference. All images are oriented with north at the top and east to the left.

We wavelength-calibrated the data, extracted the spectrum, and performed flux calibration using the *apall* package from IRAF.

Based on its LBT optical spectrum, we ruled out the AGN nature of eRASSt J1003-2607. We show in Fig. 4 and in Appendix A.12 that eRASSt J1003-2607 shows only two strong emission lines consistent with H $\beta$  and H $\alpha$  at the redshift of a nearby galaxy, NGC 3109 ( $z = 0.0014$ ). Therefore, the source is extragalactic but has a non-AGN off-nuclear origin, likely connected to an X-ray ultra-luminous object (see Sects. 6 and Appendix A.12 for a detailed discussion about off-nuclear sources and this particular object, respectively). This source is, therefore, removed from the subse-

quent discussion of SMBHBs candidates and only described in Appendix A.12.

Figure 4 shows the rest-frame optical spectra for the primary SMBHB candidates listed in Table 1. We note that, visually, some sources show broad Balmer lines, indicating the presence of a type I AGN, while others show only narrow emission lines with a galaxy-like continuum.

### 3.2.3. Optical photometric data

Optical photometric data are available for most sources, providing helpful insight into the properties of the candidates. We

**Table 2.** Optical spectral properties of the main SMBHB candidates.

Name	Telescope	Observation date	$z$	X-ray Luminosity ( $\times 10^{42}$ erg s $^{-1}$ )	SMBH mass log(M <sub>bh</sub> /M $_{\odot}$ ) (H $\beta$ ) <sup>(a)</sup>	SMBH mass log(M <sub>bh</sub> /M $_{\odot}$ ) (H $\alpha$ ) <sup>(a)</sup>
1 – eRASSt J0344-3327	NTT/EFOSC2	17/02/2024	0.090	0.25–8.21	–	(6.95 ± 2.55) <sup>(b)</sup>
2 – eRASSt J0530-4125	NTT/EFOSC2	17/02/2024	0.076	0.54–7.76	(7.26 ± 0.48)	(7.41 ± 1.21)
3 – eRASSt J1906-4850	Magellan/Baade	26/10/2021	0.049	1.73–23.80	6.63 ± 0.25 <sup>(c)</sup>	(6.72 ± 0.50) <sup>(c)</sup>
4 – eRASSt J0432-3023	SAAO	28/02/2024	0.055	0.47–9.03	7.31 ± 0.19	(7.08 ± 0.78)
5 – eRASSt J1130-0806	SAAO	28/02/2024	0.037	0.23–1.87	–	7.24 ± 0.30
6 – eRASSt J1522-3722	SAAO	19/03/2023	0.064	1.37–10.85	7.35 ± 0.09	7.17 ± 0.02
7 – eRASSt J1141+0635	NTT/EFOSC2	16/02/2024	0.101	3.28–25.64	(7.87 ± 0.55)	(7.41 ± 0.48)
8 – eRASSt J0458-2159	Magellan/Baade	11/12/2020	0.040	2.13–17.64	6.89 ± 0.05	6.85 ± 0.08
9 – eRASSt J2227-4333	6dF	29/06/2003	0.198	8.82–59.32	7.53 ± 0.22	7.46 ± 0.21
10 – eRASSt J1124-0348	NTT/EFOSC2	18/02/2024	0.021	0.02–0.77	(6.14 ± 0.9)	6.65 ± 0.18
11 – eRASSt J0036-3125	SAAO	06/09/2023	0.108	1.59–15.76	5.93 ± 0.12	7.52 ± 0.26
12 – eRASSt J1003-2607	LBT/MODS	02/01/2025	0.001	0.0007–0.005	–	–
13 – eRASSt J0818-2252	SAAO	02/12/2023	0.034	1.49–13.64	7.49 ± 0.22	(6.99 ± 0.48)
14 – eRASSt J0600-2939	SAAO	22/11/2024	0.104	1.51–17.11	–	7.47 ± 0.11
15 – eRASSt J0044-3313	SAAO	19/10/2022	0.107	2.09–20.96	7.45 ± 0.09	(6.64 ± 0.47)
16 – eRASSt J0614-3835	SAAO	30/11/2023	0.054	1.14–6.83	6.03 ± 0.16	(6.49 ± 0.58)

**Notes.** Table with sources (Column 1) and the corresponding telescopes (Column 2) and date (Column 3) from which the optical spectra were obtained. The spectroscopic redshifts (Column 4) were used to calculate the eROSITA 0.2–2.3 keV luminosities (Column 5) in the faint and bright phases of the candidates. Single-epoch SMBH masses (Columns 6 and 7) were obtained based on the spectral fit of the broad emission lines. <sup>(a)</sup> The single-epoch SMBH masses are calculated based on the scaling relations presented in [Vestergaard & Peterson \(2006\)](#) and [Mejía-Restrepo et al. \(2022\)](#) for H $\beta$  and H $\alpha$ , respectively. We report only statistical uncertainties for the SMBH mass measurements. An additional 0.3 dex should be included to consider the systematic uncertainties. <sup>(b)</sup> SMBH mass estimates in parenthesis are not well-constrained due to large uncertainties in the line measurements. <sup>(c)</sup> The source presents double-peaked broad Balmer lines.

obtained publicly available forced-photometric data on the target images from the Asteroid Terrestrial-impact Last Alert System (ATLAS, [Tonry et al. 2018](#); [Smith et al. 2020](#)) all-sky survey from their forced photometry pipeline<sup>3</sup> ([Shingles et al. 2021](#)). ATLAS allows us to have long optical photometric light curves of the candidates in the filters cyan (420–650 nm) and orange (560–820 nm). Atlas has been surveying the entire sky since  $\sim$ 2015 with a cadence of  $\sim$ 2 days. The data points were extracted by running forced photometry on the available reduced images and binned every 15 days.

We also obtained Zwicky Transient Facility (ZTF; [Masci et al. 2018](#)) optical light curves in the  $r$ -band. Since ZTF is a Northern-equatorial sky survey, only five sources have data available. The light curves are shown for these individual cases in Figs. A.1, A.2, and A.7 (see Appendix A).

### 3.3. *Swift*-UVOT data

SMBHB candidates that were observed with *Swift* (see Sect. 3.4) also have optical and UV photometric data in six filters: V, B, U, UVW1, UVM2, and UVW2 (with central wavelengths 5468, 4392, 3465, 2600, 2246, and 1928 Å, respectively) thanks to the Ultra-violet Optical Telescope (UVOT, [Roming et al. 2005](#)) mounted in the spacecraft. We obtained magnitudes and fluxes using the task UVOTSOURCE, which performs aperture photometry at the position of the source. The routine UVOTSOURCE extracts counts from an aperture of 5'' and corrects them by the background counts extracted from a 20'' circular aperture in a source-free region close to the source of interest. The UVOT light curves are shown in Figs. A.2 and A.7.

### 3.4. X-rays

We use X-ray data from several different missions, including eROSITA, *Neil Gehrels Swift Observatory* ([Gehrels et al. 2004](#)), *Neutron star Interior Composition Explorer*, and *XMM-Newton* ([Jansen et al. 2001](#)). Here, we describe their data reduction.

The eROSITA fluxes in the 0.2–2.3 keV band are extracted from the stacked eRASS:4 catalog with epoch information. For the two most extensively monitored sources, we also extract 2.3–5.0 keV and 0.2–5 keV fluxes by reducing and analyzing their eROSITA spectra (eSASS task srctool). This data is processed with the eROSITA standard processing pipeline version c020, which is based on the eROSITA Standard Analysis Software System (eSASS, [Brunner et al. 2022](#)). The source and background spectra are extracted from a 60'' circular region and a source-free annulus region with an inner radius of 140'' and an outer radius of 240'', respectively. We only retrieve X-ray spectra of the individual eRASS observations in the bright flux levels since there are not enough counts in the faint flux states of the sources. In these low-count scans, we report the corresponding eROSITA 3 $\sigma$  upper limits in the 2.3–5.0 keV and 0.2–5 keV bands.

*Swift*-XRT observations were performed during cycles 19 and 20 (Target ID: #16217, #97405) and using the director's discretionary time (DDT) in the standard photon counting (PC) mode. For each observation, we retrieve publication-ready images, light curves, and spectra, perform source detection, and obtain X-ray positions of the sources using the online *Swift*-XRT data products generator<sup>4</sup> ([Evans et al. 2007, 2009, 2014, 2020](#); [Goad et al. 2007](#)). The *Swift*-XRT data are processed using HEASOFT v6.32.

*NICER* observations were obtained during cycle 4 (#5141), cycle 6 (#7124), and with several DDT campaigns. *NICER* data were reduced with the software NICERDAS v12 distributed with

<sup>3</sup> <https://fallingstar-data.com/forcedphot/>

<sup>4</sup> [https://www.swift.ac.uk/user\\_objects/index.php](https://www.swift.ac.uk/user_objects/index.php)

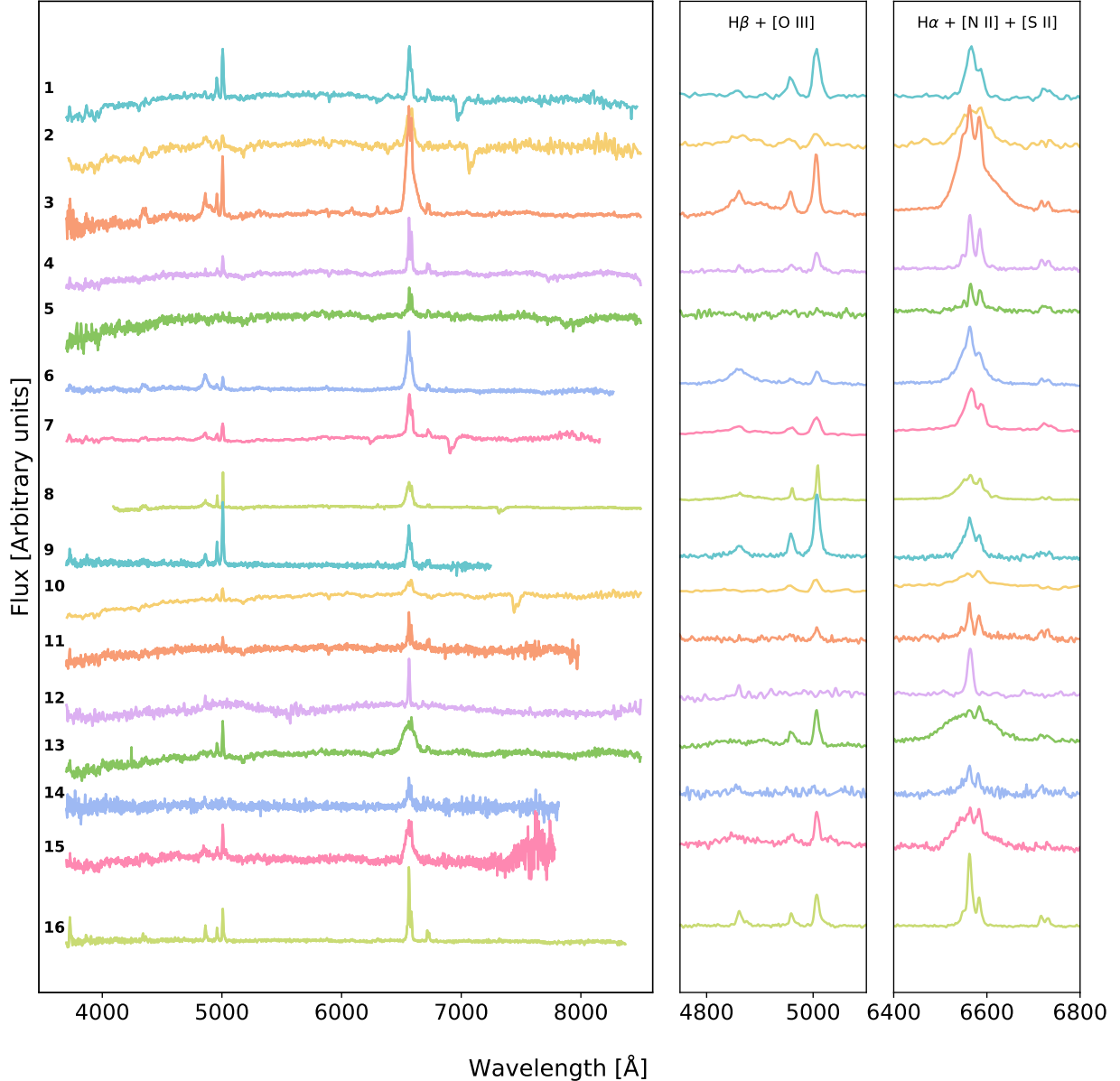


**Fig. 4.** Optical spectra compilation of the best SMBHB candidates in their rest frame. The spectra are sorted from top to bottom based on the column factor  $F$  from Table 1, described in Sect. 2.2. The middle and right panels zoom into the  $\text{H}\beta + [\text{O III}]$  and the  $\text{H}\alpha + [\text{N II}] + [\text{S II}]$  emission lines complex of each spectrum, respectively. The numbers in the plot correspond to every source listed in Table 1. The flux is given in arbitrary units where the spectra were scaled by different factors and added a constant offset of a few  $10^{-16} \text{ erg s}^{-1} \text{ cm}^{-2} \text{ Å}^{-1}$  to visualize better the different spectral shapes of the SMBHB candidates.

HEAsoft version 6.33.2. We followed the *NICER* analysis guidelines and excluded data taken during orbit day, an undershoot rate below  $300 \text{ counts s}^{-1}$ , and a default overshooting rate of less than  $30 \text{ counts s}^{-1}$  per detector. We model the background with the parameterized X-ray background model SCORPEON that consists of a non-X-ray background (NXB: related to trapped electrons, the South Atlantic Anomaly, or cosmic rays) and an astrophysical X-ray background (SKY: corresponding to Cosmic X-ray Background, diffuse local or galactic X-ray emission, solar winds, and neutral oxygen). Unlike other X-ray background library models, SCORPEON is parameterized and can be fitted together with the source model as a function of time and sky position.

We observed eRASS J1141+0635 with *XMM-Newton* (ObsID 0881880101) on 28 Dec. 2023 with a net exposure time of 112 ks. Pile-up did not affect the observations. The data was

analyzed with the *XMM-Newton* science analysis system (SAS) version 21.0.0 and HEASOFT version 6.33.2. The EPIC pn and MOS camera were operated in full-frame mode with the medium optical blocking filter. We extracted the source spectra from a  $40''$  circular aperture and the background spectra from source-free regions on the same CCD chip. For the pn camera, we selected data from pattern 0 and patterns 1–4 separately.

## 4. Data analysis

### 4.1. Full optical spectrum fitting

To characterize the nature of the sources and obtain reliable flux measurements from the broad and narrow emission lines, we correct for stellar absorption features in the spectra. We perform full spectral fitting using the pPXF package originally

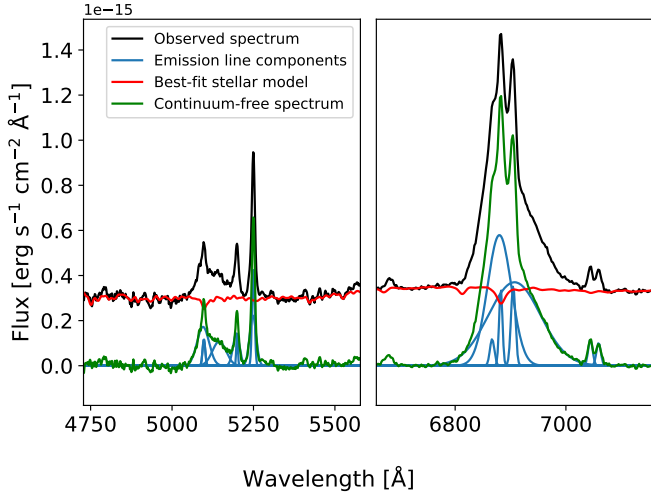


**Fig. 5.** Visualization of the full spectral fit of eRASSt J1906-4850 Magellan/Baade spectrum. The observed spectrum of the galaxy is shown in black, while the pPXF best-fit stellar model is shown in red. A continuum-free emission-line spectrum is shown in green, and the individual Gaussian components are shown in blue. We show the  $\text{H}\beta + [\text{O III}]$  complex and the  $\text{H}\alpha + [\text{N II}] + [\text{S II}]$  in the left and right panel, respectively.

described in Cappellari & Emsellem (2004) and upgraded in Cappellari (2017) and Cappellari (2023) to model and subtract the stellar contribution to obtain continuum-free emission-line spectra. The tool pPXF fits the stellar contribution to the spectrum by minimizing the residuals between the observed galaxy and the model. The model of the galaxy is defined by a convolution between stellar population templates and a line-of-sight velocity distribution (LOSVD) parametrized by a Gauss-Hermite series (see Cappellari 2017, for a detailed description of pPXF). We use single stellar populations (SSP) templates from the extended MILES (E-MILES) library, which covers the full spectral range between 1680–50 000 Å at moderately high-resolution (Vazdekis et al. 2016).

We included additive and multiplicative Legendre polynomial functions to account for discrepancies in shape between the galaxy and the templates. The degrees of the polynomial functions are chosen on a spectrum-to-spectrum basis. Since the main goal of the fit is to subtract the stellar contribution from the spectrum and not to derive stellar parameters, we choose slightly high values for the polynomial degrees (ranging between 5 and 15). We perform a regularized (regul = 100) fit where the most prominent emission lines of ionized gas and sky were previously masked. Figure 5 shows an example of the full spectral fitting routine on the Magellan/Baade spectrum of eRASSt J1906-4850. The best-fit stellar model, shown in red, is a combination of single stellar templates broadened to match the resolution of the observed spectrum. Once it is subtracted from the observed spectrum (black), we obtain the continuum-free spectrum (green) that traces the ionized gas component of the galaxy. The model is interpolated at the location of the bright emission lines that were initially masked based on the overall best stellar population fit. Thus, the continuum-free spectrum provides an absorption-corrected and model-dependent estimate of the total flux of the ionized gas lines, particularly for  $\text{H}\beta$  and  $\text{H}\alpha$ .

Considering the redshift distribution of our sources and the wavelength coverage of the spectra, we always find the following emission lines:  $\text{H}\beta \lambda 4861$ ,  $[\text{O III}] \lambda 4959, \lambda 5007$ ,  $\text{H}\alpha \lambda 6563$   $[\text{N II}] \lambda 6549, \lambda 6583$ , and  $[\text{S II}] \lambda 6717, \lambda 6730$ . These emission lines

provide valuable information about the dominant source ionizing the gas in the host galaxy. Additionally, their broad components can be used to calculate single-epoch SMBH masses.

We modeled the emission lines with Gaussian profiles using Pyspeckit, the Python Spectroscopic Toolkit package (Ginsburg & Mirocha 2011). One narrow ( $\sigma < 500 \text{ km s}^{-1}$ ) Gaussian component was used to fit each of the mentioned emission lines in each spectrum. Additionally, to reproduce the Broad Line Region (BLR) emission of the Balmer lines, we incorporated one broad ( $300 < \sigma < 3300 \text{ km s}^{-1}$ ) component for  $\text{H}\beta$  and one for  $\text{H}\alpha$ . We fixed the ratios of the  $[\text{O III}]$  and  $[\text{N II}]$  doublet to their theoretically determined values of 3 (Osterbrock & Ferland 2006) to reduce the degrees of freedom of the fit. Since the spectral resolutions of our spectra are variable depending on the used instrument, we usually cannot separate the  $\text{H}\alpha$  component from the  $[\text{N II}]$  lines accurately. Therefore, we use the strong and well-isolated  $[\text{O III}] \lambda 5007$  line as a template to define the widths for all the narrow lines, particularly the  $[\text{N II}]$  lines. This choice does not leave significant residuals in the other lines. The emission line fitting process is also shown in Fig. 5. We note that eRASSt J1906-4850 can only be well-fitted with two broad Gaussian components per Balmer line and an extra, broader, and blue-shifted component for the  $[\text{O III}]$  lines. Similarly, eRASSt J1522-3722 needs two Gaussian components to fit the broad and asymmetric  $[\text{O III}] \lambda 5007$  line.

We obtained the flux, velocity, and velocity dispersion in the line-of-sight of the ionized gas based on the zeroth, first, and second moment of the Gaussian profiles. Once we performed an initial fit, we retrieved reliable error measurements to these quantities using a bootstrapping technique. We resample the residuals, assuming they are Gaussian distributed and centered in the flux of the model. We added these new residuals to the initial best-fit model of the emission lines and performed a new fit. We repeated this process 1000 times and stored the fluxes, velocities, and velocity dispersions of each realization. Thus, the final emission line measurement will be given by the median and standard deviation of the 1000 realizations. We obtained reliable redshifts based on the wavelength shift of the narrow  $[\text{O III}] \lambda 5007$  Å emission line and the 1000 realizations of the bootstrapping method. The typical errors on the redshifts are on the order of  $\sim 10^{-5}$ . These redshifts are reported in Table 2 (Column 3), and they were also used to compute the X-ray luminosity of the SRG/eROSITA data (Column 4).

#### 4.2. X-ray data analysis

The SRG/eROSITA, *Swift*-XRT, *NICER*, and *XMM-Newton* spectra were fitted using the Python interface of the XSPEC (Arnaud 1996) spectral-fitting program, PyXspec. We used Poisson statistics (Cash 1979), cosmic abundances from Wilms et al. (2000), and photoelectric absorption cross sections provided by Verner et al. (1996); also, we quote all the X-ray parameter errors at the  $1\sigma$  (68%) confidence level. Typical requested exposure times for *Swift*-XRT and *NICER* spectra are 3 and 8 ks, respectively. We fit the spectra and obtain X-ray fluxes using a single power-law model with a fixed Galactic absorption ( $\text{tbabs}_{\text{Gal}} * \text{powerlaw}$ ) that depends on the position on the sky of the SMBHB candidate and is obtained from measurement of the Galactic neutral atomic hydrogen column density<sup>5</sup> (HI4PI Collaboration 2016). We also fit an absorbed power-law ( $\text{tbabs}_{\text{Gal}} * \text{tbabs}_{\text{intr}} * \text{powerlaw}$ ) to the different spectra to test

<sup>5</sup> <https://heasarc.gsfc.nasa.gov/cgi-bin/Tools/w3nh/w3nh.pl>

for the intrinsic absorption of the X-ray sources. Spectral parameters such as the intrinsic column density  $N_H$ , photon index  $\Gamma$ , and hardness ratio were calculated for every observation. The hardness ratio ( $HR = (\text{hard} - \text{soft})/(\text{hard} + \text{soft})$ ) was calculated using the soft (0.2–2.3 keV) and hard (2.3–5.0 keV) energy bands defined by the eROSITA bands. Figures 7 and 8 show the light curves of the monitored objects with fluxes and luminosities retrieved from the different X-ray missions. The observed luminosities were computed by considering the luminosity distance of each source, which depends on the optical redshift and the assumed  $\Lambda$ CDM cosmology (Hinshaw et al. 2009).

#### 4.3. Stacked X-ray analysis

We stacked the *NICER* and *Swift*-XRT observations of each source to constrain their time-averaged spectral properties. *NICER* observations were stacked using the NICERDAS v12 tool `niobsmerge` that combines cleaned and calibrated products of several observation segments. *Swift*-XRT stacked spectra were directly downloaded from the Living Swift XRT Point Source Catalogue (LSXPS; Evans et al. 2023). LSXPS is a living catalog that gets updated in nearly real-time and contains position, fluxes, spectral details, and variability information for hundreds of thousands of X-ray point sources detected by the Swift X-ray Telescope.

We considered two simple X-ray models to study properties like the line-of-sight absorption and the overall spectral shape of the source. We fit a redshifted power-law absorbed by Galactic and intrinsic hydrogen atoms ( $\text{tbabs}_{\text{Gal}} * \text{tbabs}_{\text{Intr}} * \text{zpowerlaw}$ ) and an absorbed thermal accretion disk consisting of multiple blackbody components ( $\text{tbabs}_{\text{Gal}} * \text{tbabs}_{\text{Intr}} * \text{diskbb}$ ).

## 5. Results

### 5.1. Optical

We confirm that 15 out of the 16 observed SMBHB candidates are extragalactic sources with redshifts ranging between  $z \sim 0.02$ –0.2. Most of the sources display bright emission lines such as [O III], H $\alpha$ , and [N II] and a unique variety of line profiles, especially in the broad components.

The Baldwin, Phillips & Telervich (BPT; Baldwin et al. 1981) diagram considers optical emission-line flux ratios to provide a unified classification of the nature of the dominating ionization mechanism (Baldwin et al. 1981; Veilleux & Osterbrock 1987; Kewley et al. 2000, 2001, 2006). Figure 6 shows the [N II]-BPT diagnostic diagram for the spectroscopically observed sources. The region delimited by the blue (denoted as Ka03, Kauffmann et al. 2003) and the black curve (Ke01 in the diagram, Kewley et al. 2001) is defined as a composite region where AGN and SF can be responsible for the ionization of the gas in the host galaxy. Despite all of the sources being X-ray selected, we note that not all of them show strong AGN features based on their optical spectra and their location on the BPT diagram. eRASSt J0530-4125 (#2 in the diagram) displays a galaxy-like spectrum with noticeable stellar absorption features and a weak H $\beta$  broad emission line. On the other hand, eRASSt J1522-3722 (#6 in the diagram) shows strong broad components proper of AGN. However, the source falls into the star-forming portion of the diagram because the [O III] emission line was fitted with two Gaussian components due to the line being broad and asymmetric. Therefore, at the moment of taking the flux ratio, only the bright and narrower component was considered. Broad and

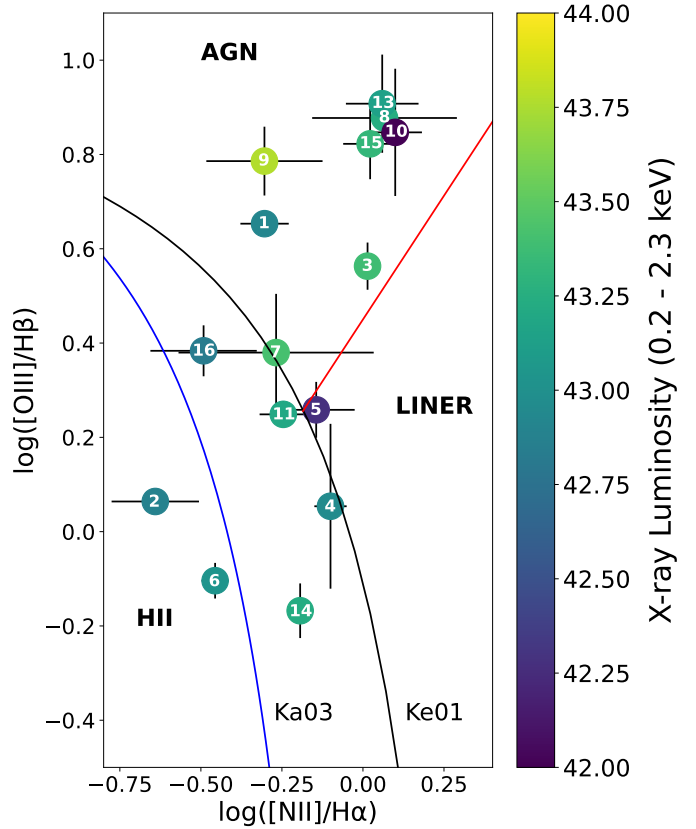


**Fig. 6.** [N II]-BPT ( $[\text{O III}]\lambda 5007/\text{H}\beta$  versus  $[\text{N II}]\lambda 6583/\text{H}\alpha$ ) diagnostic diagram for the SMBHB candidates. The black curve marks the separation proposed by Kewley et al. (2001, denoted as Ke01 in the diagrams), between the theoretical maximum ionization driven by pure star-formation in HII regions and those regions ionized by AGN. The red solid line on the BPT diagram marks the separation between AGN and Low Ionization Narrow Emission-line Regions (LINERs), as proposed by Schawinski et al. (2007), while the blue solid curve represents the separation between AGN and star formation reported by Kauffmann et al. (2003) denoted as Ka03 on the [NII]-BPT diagram. The markers are color-coded according to the observed eROSITA luminosity of the bright level in the 0.2–2.3 keV band. The numbers of the markers correspond to the sources listed in Table 1.

asymmetric [O III] $\lambda 5007$  lines could indicate the presence of outflows in the nuclear region of the galaxy.

Following the  $M_{\text{bh}} - \text{H}\beta$  and  $M_{\text{bh}} - \text{H}\alpha$  scaling relations from Vestergaard & Peterson (2006) and Mejía-Restrepo et al. (2022), respectively, we calculate single-epoch SMBH masses assuming that the broad line region size is larger than any binary separation and that the gas is virialized around the central black hole(s). The SMBH masses of the candidates based on the FWHM and luminosity of the broad H $\beta$  and H $\alpha$  lines are presented in Table 2. Sources without SMBH mass measurements do not show significant broad H $\beta$  in their spectrum. Instead, we derive SMBH masses using the H $\alpha$  line, following Mejía-Restrepo et al. (2022). eRASSt J1906-4850 is the only source with a particularly interesting double-peaked broad Balmer profile, as shown in Fig. 5. We derive a velocity shift of  $\Delta v = 2915 \pm 736 \text{ km s}^{-1}$  based on the wavelength separation of the corresponding line centroids.

Based on their spectroscopic observations, we confirm that all objects (except eRASSt J1003-2607, which displays an off-nuclear nature) are extragalactic sources. The galaxies show evi-

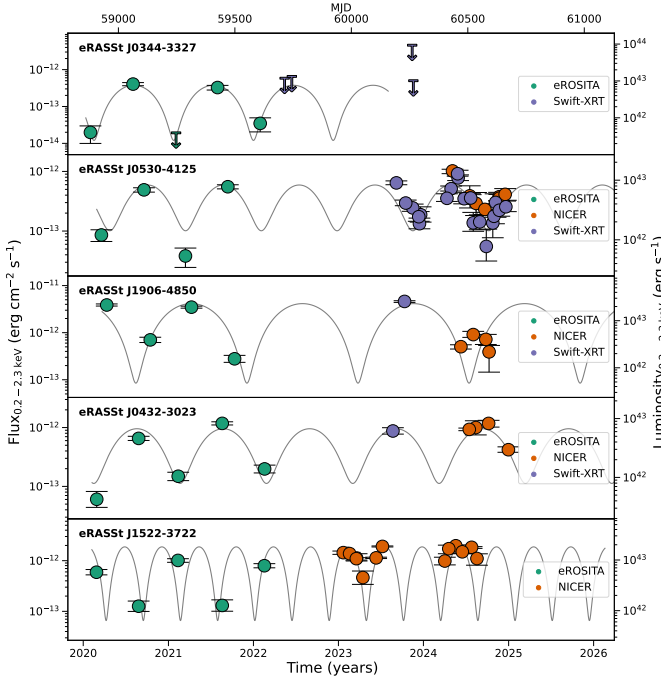


**Fig. 7.** X-ray light curves of the X-ray monitored SMBHB candidates. SRG/eROSITA, *Swift*-XRT, and *NICER* data are shown in green, purple, and orange, respectively. We display a sinusoidal curve (gray) to visualize the contrast between the observed X-ray variability and periodically variable signal. The secondary y-axis shows the observed frame 0.2–2.3 keV X-ray luminosities of the sources based on their observed X-ray fluxes and redshifts derived from their optical spectra.

dence of AGN activity with relatively low single-epoch SMBH masses ( $\sim 10^7 M_\odot$ ). Sources falling into the composite and the star-forming regions of the BPT diagram have typical X-ray luminosities on the order of  $10^{43}$  erg s $^{-1}$  in the 0.2–2.3 keV, suggesting that the mechanism ionizing the gas in the host galaxy is unrelated to the X-ray emitting source. See Sect. 6.2 for a detailed discussion on the origin of the X-rays in our sources.

## 5.2. X-rays

Figures 7 and 8 compile every X-ray observation performed during our search for periodically varying light curves. We only show the sources that were observed before Dec. 31st, 2024.

The observed-frame 0.2–2.3 keV X-ray luminosities of the monitored galaxies range between  $10^{42}$ – $10^{43}$  erg s $^{-1}$ . These values strongly suggest that the X-ray emission is produced by accretion onto the SMBH in the center of the galaxy since no other objects or phenomena in the host galaxy can produce such energetic and persistent X-ray emission. We note that some sources support the quasiperiodic behavior seen in Figs. 7 and 8. However, longer X-ray monitoring programs are needed to confirm or rule out the periodic nature of the sources. We emphasize that since there are sources with few X-ray data points, the tentative periodicities are mainly driven by the eROSITA data points. A stringent periodic analysis should be performed with a well and more populated light curve.

We display a sinusoidal curve (gray) based on the period found by the Lomb-Scargle periodogram (Lomb 1976; Scargle 1982). This periodogram technique is designed to detect periodic signals in unevenly spaced observations. The period of the sinusoidal curve is obtained from the frequency at which each

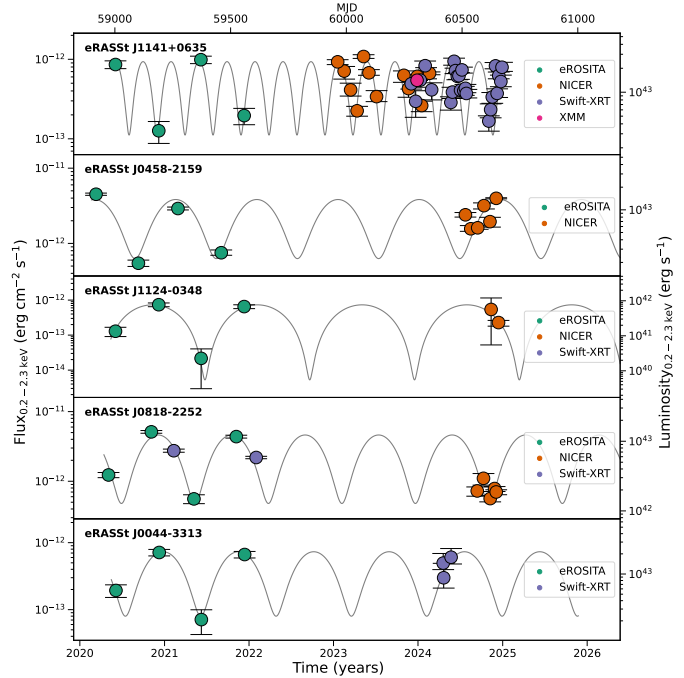


**Fig. 8.** Continuation of Fig. 7. X-ray light curves of the second half of the X-ray monitored SMBHB candidates.

source has a maximum in their periodogram. We emphasize that this curve is only to guide the visualization of the tentative periods and highlights the contrast between the X-ray variability and the periodic curve. We also emphasize that the periods derived might not be statistically significant since the number of data points are still insufficient to perform a proper modeling and false-positive probability analysis of the periodogram. The periodogram is designed to find periods in light curves by comparing the observed signal against pure white noise (null hypothesis of not having any signal at all). However, AGNs are variable, and their variability is stochastic, dominated by red noise. Therefore, using the periodogram to confirm periodicities in AGN should be accompanied by a detailed analysis that considers the red noise as a null hypothesis, as described in Vaughan (2005). See Sect. 6.1 for a detailed discussion of red noise and stochastic AGN variability.

### 5.2.1. The two most well-monitored sources in X-rays

eRASSt J0530-4125 (#2) and eRASSt J1141+0635 (#7) are the two most well-monitored sources in our SMBHB candidate sample. Here, we present extended X-ray properties for these objects, and we discuss their X-ray variability.

*eRASSt J0530-4125*: The source displays an interesting variability pattern that seems to be persistent, even after two years of the last eRASS4 observation. Figure 9 shows the soft (0.2–2.3 keV), hard (2.3–5.0 keV), and total (0.2–5.0 keV) X-ray light curve for eRASSt J0530-4125. The light curves in different energy bands follow the same trend, indicating that the variability is not produced by changes in the spectral shape. This is also visualized in the subsequent panels where the column density,  $n_H$ , photon index,  $\Gamma$ , and hardness ratio are rather constant in time. Apparent outliers in the column density and photon index measurements are associated with low exposure times while in the faint flux state, therefore having large uncertainties.

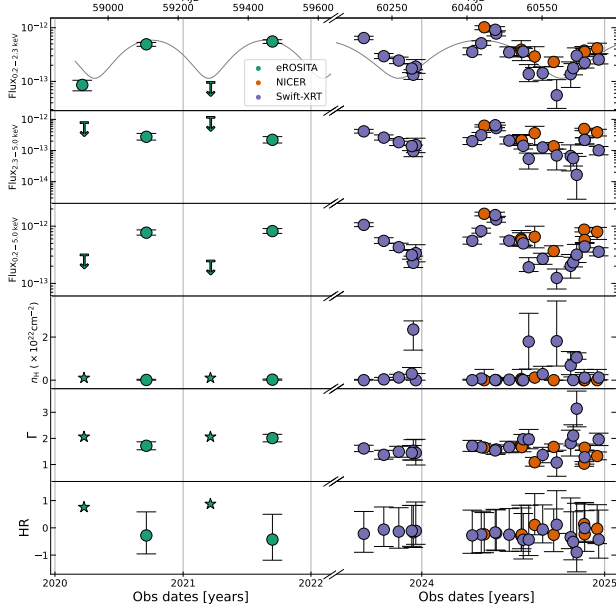


**Fig. 9.** X-ray properties of eRASSt J0530-4125 observed with eROSITA, *Swift*-XRT, and *NICER*. Light curves at 0.2–2.3 keV, 2.3–5.0 keV, and 0.2–5.0 keV bands are shown in the first, second, and third panels, respectively. Spectral X-ray properties such as intrinsic  $N_{\text{H}}$ , photon index  $\Gamma$ , and hardness ratio are also shown in the fourth, fifth, and sixth panels.

The X-ray light curve reveals a tentative quasiperiodic variability with a period of  $\sim 12$  months, as highlighted with the gray sine curve in the top panel of Fig. 9. We emphasize that the periodic signal needs to be carefully tested and interpreted. We do not discard the possibility that the variability pattern is the result of stochastic processes (see also Sect. 6.1).

In the case that the periodic signal is caused by a SMBHB, we can derive the distance between the SMBHBs. Assuming a 12-month period and a combined SMBHB mass of  $10^{7.26} M_{\odot}$  (Table 2), the distance would be 1.2 milli-pc (considering a Keplerian orbit:  $d = [GM_0^2/4\pi^2]^{1/3}$ ; where  $d$  is the distance,  $M$  is the total mass of both SMBHBs,  $P_0$  is the measured period, and  $G$  is the gravitational constant). We obtain an orbital velocity of  $v \sim 8000 \text{ km s}^{-1}$ , using  $v = 2\pi d P^{-1}$  (Serafinelli et al. 2020). The velocity can also be used to estimate the energy shift of the 6.4 keV Fe  $\text{K}\alpha$  lines in the X-ray spectrum. We find that  $\Delta E_{\text{Fe K}\alpha} = 0.17 \text{ keV}$ . This energy shift would barely be resolved by *XMM-Newton*.

**eRASSt J1141+0635:** The *SRG*/eROSITA data of this source shows a clear “up-down-up-down” pattern (see Fig. 10). However, the *NICER* monitoring (orange markers in Fig. 8) suggests a more complex X-ray variability where the flux decreases in a timescale of three months and rises again after one month. Until the first half of 2023, the data matched the periodic behavior of the sinusoidal curve with a period of  $T \sim 120$  days.

At later times, any hint of periodic variability is lost. On 28 Dec. 2023, we obtained a pre-approved AO20 ToO *XMM-Newton* observation for a net total of 112 ks, aiming to detect a double-peaked profile in the Fe  $\text{K}\alpha$  emission line. We detect a faint and barely resolved emission line at an observed line energy of  $E_{\text{line}} = 6.22^{+0.29}_{-0.24} \text{ keV}$ , a width of  $\sigma_{\text{line}} = 0.8^{+0.3}_{-0.2} \text{ keV}$ , and normalization of  $n_{\text{line}} = 3.54^{+1.0}_{-0.9} \times 10^{-6} \text{ photons cm}^{-2} \text{ s}^{-1}$ . A detailed analysis of the *XMM-Newton* observation will be presented in future works.

eRASSt J1141+0635 was further monitored during *Swift*-XRT cycle 20 with a cadence of one week. The high-cadence

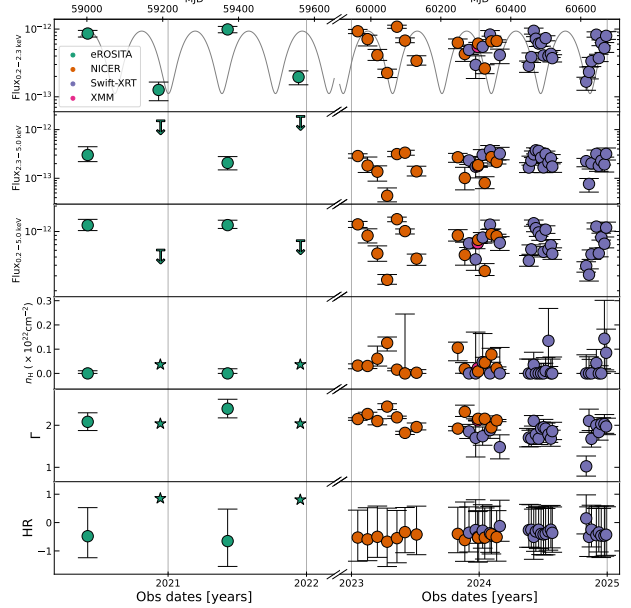


**Fig. 10.** X-ray properties of eRASSt J1141+0635 observed with eROSITA, *NICER*, *Swift*-XRT, and *XMM-Newton*. The panels are similar to those shown in Fig. 9.

*Swift*-XRT data show a more structured variability than in the previous observation block; however, it is unclear whether or not the initial quasiperiodic signal detected with *NICER* is again present. Further X-ray observations are needed to disentangle the nature of this source. If the source is confirmed to be a SMBHB by future observations, the disappearance of the periodic signal could imply that the accretion of matter in binaries is not always stable and that there could be episodes of less or more accretion that would disrupt the periodic behavior of the sources.

## 5.2.2. Stacked X-ray properties of the sample

The time-averaged X-ray spectra were also analyzed to study the spectral shape properties of the sources. Stacking the available data increases the signal-to-noise of the observations and can provide valuable information about their nature. Table 3 summarizes the best-fit values for the two models tested. The models have a fixed Galactic absorption component ( $\text{tbabs}_{\text{Gal}}$ ) derived from the HI4PI Collaboration (2016). We note that all sources have low intrinsic absorption and are mostly well characterized by power-law models with typical AGN-like photon index ( $\Gamma \sim 2$ ). Only one object (eRASSt J0344-3327) shows a soft power law, likely associated with the tidal disruption event (TDE) nature of the source (see Appendix A).

## 6. Discussion

### 6.1. Stochastic AGN variability as a source of quasiperiodic light curves

Throughout the paper, we have been cautious with interpreting the quasiperiodic signals displayed by the galaxies as SMBHBs since single-SMBHB accretion is stochastic and can display artificial periodic features. Here, we give a more detailed explanation of the red-noise phenomena and emphasize that in the second paper of this program, we will properly quantify the effect of stochastic accretion in our sample (Tubín-Arenas et al., in prep.).

**Table 3.** Stacked X-ray spectral properties of the monitored SMBHB candidates.

Source <sup>(a)</sup>	Obs.	Exposure (s)	$N_{\text{H}}^{(b)}$ ( $\times 10^{20}$ cm $^{-2}$ )	tbabs <sub>Gal</sub> *tbabs <sub>Intr</sub> *zpowerlaw			$N_{\text{H}}$ ( $\times 10^{20}$ cm $^{-2}$ )	tbabs <sub>Gal</sub> *tbabs <sub>Intr</sub> *diskbb		
				$\Gamma$	Norm. ( $\times 10^{-4}$ )	stat/d.o.f. = $\chi^2$		T <sub>in</sub> (eV)	Norm.	stat/d.o.f. = $\chi^2$
1	<i>NICER</i>	15981	$1.57^{+1.41}_{-1.57} \text{ (c)}$	$5.35^{+1.64}_{-0.94}$	$2.13^{+2.13}_{-1.49} \times 10^{-2}$	$180.33/144 = 1.25$	$0.0^{+0.0}_{-0.0}$	$69^{+11.6}_{-9.93}$	$5.24^{+8.18}_{-3.02} \times 10^2$	$180.16/147 = 1.23$
2	<i>NICER</i>	35802	$4.48^{+0.6}_{-0.48}$	$1.97^{+0.06}_{-0.05}$	$1.99^{+0.05}_{-0.05}$	$251.61/169 = 1.49$	$0.0^{+0.0}_{-0.0}$	$478^{+13}_{-12}$	$0.48^{+0.05}_{-0.05}$	$305.93/173 = 1.77$
	<i>Swift</i> -XRT	70119	$0.0^{+0.0}_{-0.0}$	$1.67^{+0.08}_{-0.07}$	$1.22^{+0.08}_{-0.07}$	$697.14/1020 = 0.68$	$0.0^{+0.0}_{-0.0}$	$1260^{+12}_{-66}$	$113^{+2.5}_{-20}$	$750.66/1020 = 0.74$
3	<i>NICER</i>	24130	$19.3^{+2.42}_{-11.2}$	$2.84^{+0.19}_{-0.18}$	$3.19^{+0.19}_{-0.19}$	$246.64/176 = 1.40$	$5.92^{+99.4}_{-2.75} \times 10^5$	$998^{+514}_{-991}$	$4.72^{+200000}_{-2.39} \times 10^{11}$	$349.12/180 = 1.94$
4	<i>NICER</i>	40670	$0.75^{+0.75}_{-0.75}$	$1.94^{+0.38}_{-0.38}$	$1.85^{+0.045}_{-0.045}$	$241.88/181 = 1.34$	$0.0^{+0.0}_{-0.0}$	$353^{+8.12}_{-8.36}$	$1.44^{+0.141}_{-0.14}$	$238.09/185 = 1.29$
6	<i>NICER</i>	63663	$0.0^{+3.87}_{-0.0}$	$2.06^{+0.05}_{-0.05}$	$6.52^{+0.09}_{-0.09}$	$233.7/171 = 1.37$	$0.0^{+0.0}_{-0.0}$	$539^{+4.63}_{-4.32}$	$0.98^{+0.03}_{-0.03}$	$700.15/175 = 4.00$
7	<i>NICER</i>	108169	$3.82^{+0.14}_{-0.39}$	$2.26^{+0.02}_{-0.02}$	$4.27^{+0.03}_{-0.03}$	$528.7/186 = 2.84$	$0.0^{+0.0}_{-0.0}$	$354^{+3.21}_{-1.74}$	$3.46^{+0.07}_{-0.12}$	$1922.37/190 = 10.12$
	<i>Swift</i> -XRT	89832	$0.0^{+2.22}_{-0.0}$	$1.8^{+0.05}_{-0.05}$	$1.91^{+0.09}_{-0.08}$	$766.03/1020 = 0.75$	$0.0^{+0.0}_{-0.0}$	$1060^{+3.38}_{-3.36}$	$3.15^{+0.4}_{-0.4} \times 10^{-2}$	$989.81/1020 = 0.97$
	<i>XMM-Newton</i>	112600	$2.75^{+0.2}_{-0.18}$	$2.3^{+0.05}_{-0.04}$	$2.23^{+0.08}_{-0.07}$	$8601.12/9166 = 0.94$	$0.0^{+0.0}_{-0.0}$	$426^{+0.2}_{-0.53}$	$0.96^{+0.005}_{-0.005}$	$14694.14/9166 = 1.60$
8	<i>NICER</i>	39761	$0.0^{+0.0}_{-0.0}$	$1.95^{+0.02}_{-0.03}$	$9.11^{+0.02}_{-0.07}$	$219.20/185 = 1.18$	$0.04^{+0.49}_{-0.04}$	$463^{+4.8}_{-4.88}$	$2.61^{+0.11}_{-0.11}$	$546.38/189 = 2.89$
10	<i>NICER</i>	17335	$6.36^{+2.76}_{-2.36}$	$1.34^{+0.15}_{-0.12}$	$1.23^{+0.061}_{-0.071}$	$228.17/155 = 1.47$	$0.04^{+0.43}_{-0.04}$	$1030^{+7.12}_{-9.93}$	$2.35^{+0.88}_{-0.48} \times 10^{-2}$	$231.39/158 = 1.46$
13	<i>NICER</i>	31238	$5.56^{+8.64}_{-3.43}$	$2.03^{+0.14}_{-0.13}$	$3.70^{+0.16}_{-0.14}$	$250.41/176 = 1.42$	$2.06^{+97.90}_{-4.43} \times 10^4$	$1000^{+17.60}_{-3.95} \times 10^3$	$1.0^{+10000}_{-0.9} \times 10^{20}$	$501.73/180 = 2.79$

**Notes.** <sup>(a)</sup> The number of the sources refer to Table 1. <sup>(b)</sup> Intrinsic column density. <sup>(c)</sup> The errors in the measurements correspond to the 68% confidence interval.

Accretion onto single SMBHs produces highly variable and aperiodic X-ray emission with a stochastic behavior: the so-called red noise (see, e.g., [Press 1978](#); [Vaughan et al. 2003](#)). The power spectral density (PSD) indicates how strong the variability is as a function of temporal frequency (timescale $^{-1}$ ), and it has been used to study variability across different timescales. In red-noise-dominated sources, the X-ray PSD of these light curves is commonly represented by a power law with slopes ranging between 1–2 ([Lawrence et al. 1987](#); [McHardy & Czerny 1987](#); [Markowitz et al. 2003](#); [McHardy et al. 2006](#); [Paolillo et al. 2023](#)), opposed to random white-noise PSDs with slope values near zero.

The search for periodic AGN features has been limited by the data quality and poor time resolution of the observations. Additionally, single-AGN stochastic variability can mimic quasiperiodic variability ([Krishnan et al. 2021](#); [Witt et al. 2022](#)). [Vaughan et al. \(2016\)](#) claim that the periodic variability of the quasar PG 1302-102 found by [Graham et al. \(2015\)](#) can be explained by stochastic variability. They also found a few-cycle “phantom” periodicities in simulated red-noise light curves based on steep PSD shapes. “Phantom” periodicities are found in large optical quasar surveys (see, e.g., [MacLeod et al. 2010](#)) where the tentative periods of the light curve tend to be similar to the total length of the observations ([Vaughan et al. 2016](#)). False positives can be reduced by investigating the range of parameter space in which binary systems can be detected. [Krishnan et al. \(2021\)](#) found that discarding timescales greater than (roughly) 1/3 of the total observation length is an effective way to reduce false positives. [Witt et al. \(2022\)](#) found that periodic signals are more easily detectable if the period is short or the amplitude of the signal is large compared to the contribution of the noise.

We cannot rule out the presence of red-noise variability in our sample until further follow-up campaigns provide strong evidence of either periodic or stochastic variability. Real periodic processes should continue to show periodic behavior in future observations, while AGNs dominated by red-noise processes will gradually deviate from the periodic scenario. Therefore, continuous and extended X-ray monitoring programs will be needed when searching for periodic light curves that are expected of SMBHBs.

We will investigate in detail the effect of red-noise-induced variability in the selection of our sources by obtaining false positive rates (Paper II). These rates will be computed by simulating millions of pure red-noise light curves and over-imposing the *SRG*/eROSITA scanning pattern (i.e., one datapoint every six months). Thus, we will identify the number of spurious sources

that show the same variability pattern selected in this paper. We will also include quasiperiodic signals mixed with different PSD slopes and red-noise levels to test our selection method of the *SRG*/eROSITA candidates. These results will be presented in Paper II (Tubín-Arenas et al., in prep.).

## 6.2. Possible origin of the X-ray quasiperiodicity in our sample

In the following section, we assume that the quasiperiodic signatures found in the X-ray light curves are not caused by red noise but are real. Given the obtained multiwavelength data, we discuss which scenarios are still plausible for the individual sources. These scenarios include off-nuclear sources, objects interacting with the central SMBH (e.g., TDEs and QPs), and SMBH binaries. Under each scenario, we explain why we consider it for the given source. To summarize our current understanding of our sources, we give an overview of the already excluded and still possible scenarios in Table 4. If several scenarios are still listed for a source, the current data do not allow us to favor one possible scenario over another.

**Off-nuclear sources:** Ultra-luminous X-ray sources are extragalactic objects located outside the nucleus of the host galaxy with bolometric luminosities ranging between  $10^{38}$  and  $10^{42}$  erg s $^{-1}$ . The most extreme cases are also known as hyper-luminous objects (HLXs). The source population of ULXs and HLXs are expected to be diverse, covering both neutron-star binaries and black-hole binaries ([Kaaret et al. 2017](#); [Gong et al. 2016](#)). However, HLXs are more likely to require an intermediate-mass black hole (IMBH) to power their emission ([Webb et al. 2012](#)). The brightest known HLX is HLX-1, located in ESO 243-49. It has a maximum 0.2–10 keV luminosity of  $\sim 10^{42}$  erg s $^{-1}$  ([Farrell et al. 2009](#)). This luminosity range is of particular interest as it covers the overlap of ULXs and low-luminosity AGN. Additionally, the X-ray light curve of HLX-1 shows possible recurrence in its variability (see, e.g., [Lasota et al. 2011](#); [Servillat et al. 2011](#)), which could be interpreted as “up-down” patterns when sampled with low cadence, such as with *SRG*/eROSITA. Therefore, HLXs could contaminate our sample, given their luminosity and variability.

Two of the most used methods to discard the presence of HLXs in our sample are X-ray positions and luminosities. HLXs are expected to be off-nuclear sources, so precise X-ray positions compared against the optical position of the galactic nuclei

**Table 4.** Light curve status and possible nature of the primary sample of SMBHB candidates.

Source	Light curve status			Possible nature of the X-ray emission		
	eROSITA only	eROSITA + short program	eROSITA + long-term program	Periodic signal	HLXs	TDEs&QPEs
1		✓				✓/✓
2			✓	✓		✓
3		✓				✓/✓
4		✓		✓		✓/✓
5	✓			✓	✓	✓/✓
6			✓	✓		✓
7			✓	✓		✓
8		✓		✓		✓/✓
9	✓			✓		✓/✓
10		✓			✓	✓/✓
11	✓			✓		✓/✓
12			✓	✓	✓	
13		✓		✓		✓/✓
14	✓			✓		✓/✓
15	✓			✓		✓/✓
16	✓		✓			✓/✓

**Notes.** Summary of the X-ray monitoring campaigns for each source and their tentative nature. We categorized the sources according to their number of X-ray follow-ups. eROSITA-only (Column 2) are sources that only have eROSITA data and will be observed in future programs. eROSITA+short program (Column 3), and eROSITA+long program (Column 4) are the sources where we have less or more than six X-ray pointings after the eROSITA data, respectively. We mark as periodic signals (Column 5) those sources where the data do not rule out the possibility of periodicity. This column also includes sources where we only have eROSITA data since more data are required to confirm or rule out quasiperiodic signals. The possible nature of the sources is divided into three categories. HLXs (Column 6), nuclear transients (e.g., TDEs & QPEs; Column 7), and SMBHBs (Column 8). We mark the sources where the data have not entirely ruled out the possibility that the source possesses a given nature.

can provide an initial assessment of the nature of these objects. Figure 3 and Table 1 show the separation, in arcseconds, between the optical *Gaia* positions, centered in the nuclei of the galaxies and the position of the X-ray emission. All of the candidates have X-ray emissions consistent with being emitted by the central parts of the galaxy (except for eRASSt J1003-2607. See Appendix A). The sources with the largest separation (eRASSt J1130-0806 and eRASSt J0600-2939, separated by 2°33' and 2°88', respectively) are still consistent with being nuclear within the eROSITA positional uncertainty. However, we note that this method does not discard off-nuclear sources with projected separations smaller than the X-ray spatial resolution. Most of the luminosities in the faint flux state of our sources listed in Table 2 are consistent with the maximum luminosity of HLX-1. However, when considering the observed luminosities (only between 0.2–2.3 keV) of our candidates in the bright phase, we note that all of the galaxies (except for eRASSt J1130-0806 and eRASSt J1124-0348) are almost one order of magnitude brighter than HLX-1. Therefore, the luminosity argument makes it unlikely that the X-ray origin in our sources comes from an off-nuclear, close-to-center HLX object. We show in Table 4 the two sources from our sample that could be HLXs based on their 0.2–2.3 keV X-ray luminosities in their bright states (eRASSt J1130-0806 and eRASSt 1124-0348). The HLX scenario for object eRASSt J1003-2607 is supported by its X-ray luminosity and its off-center position. Since the X-ray luminosities of eRASSt J1130-0806 and eRASSt 1124-0348 are also consistent with the ranges expected for low luminosity AGN, we still consider them under the other possible scenarios. If they are of HLX origin, it is interesting to note that they would be among the most luminous HLXs ever detected.

*Objects interacting with the central SMBH:* (i) TDEs produce energetic flares originating in the nuclei of galaxies due to the accretion of disrupted stellar debris onto the SMBH. TDEs usually display soft, thermally dominated X-ray spectra,

and their light curves typically display a sharp rise in brightness followed by a slow decline with timescales of months or years ( $\propto t^{-5/3}$ ) (see [Saxton et al. 2020](#); [Gezari 2021](#), and reference therein). Lately, more exotic phenomena, such as repeating TDEs, have been discovered (see, e.g., [Payne et al. 2021](#); [Liu et al. 2023, 2024](#); [Malyali et al. 2023](#)). In this scenario, the star survives the first encounter with the SMBH and only loses a fraction of its mass. The system will produce new accretion events in the subsequent encounters with the SMBH. The recurrence time of the X-ray flares in the known pTDEs ASASSN-14ko ([Payne et al. 2021](#)) and eRASSt J045650.3-203750 ([Liu et al. 2023, 2024](#)) are consistent with the timescales probed by our SMBHB search with timescales of 100–300 days, respectively.

(ii) Quasi-periodic eruptions (QPEs) are newly discovered X-ray transients that originate in the nuclei of nearby galaxies where only the X-ray light curve shows persistent, soft, repeating, and narrow X-ray flares with timescales of hours to weeks (see, e.g., [Miniutti et al. 2019, 2023](#); [Giustini et al. 2020](#); [Arcodia et al. 2021, 2024](#); [Quintin et al. 2023](#); [Nicholl et al. 2024](#); [Guolo et al. 2024](#)). Possible scenarios to explain QPEs are accretion disk instabilities (e.g., [Pan et al. 2022](#)) or stellar objects impacting the accretion disk of the SMBH in close and elliptical orbits ([Xian et al. 2021](#)). QPEs and TDEs have been found to prefer similar host galaxies ([Wevers et al. 2022, 2024](#), and references therein). Additionally, QPEs have been detected in galaxies years after TDEs ([Miniutti et al. 2023](#); [Quintin et al. 2023](#); [Nicholl et al. 2024](#); [Pasham et al. 2024](#)), suggesting a connection in the formation mechanism of both transients. In this scenario, a main-sequence star (brought into the nucleus as an extreme mass-ratio inspiral; EMRI) emits flares every time it crosses the accretion disk formed by the debris of a TDE ([Linial & Metzger 2023](#); [Suková et al. 2024](#)).

Repeating X-ray transients (such as TDEs and QPEs) could potentially explain the initial pattern of the

SRG/eROSITA-selected objects in this work. Repeating TDEs present longer timescales, consistent with the timescales of our SMBHB search. In fact, the source with the largest ratio between the faint and bright X-ray states in our sample (eRASSt J0344-3327) is likely a TDE, based on the sharp rise and slow decline in its optical and IR light curves, as well as its steep and soft X-ray spectrum (see Fig. A.1). Other sources such as eRASSt J1906-4850 (Fig. A.3), eRASSt J1130-0806 (Fig. A.5), eRASSt J1124-0348 (Fig. A.10), eRASSt J0036-3125 (Fig. A.11), and eRASSt J0044-3313 (Fig. A.16) show weak but noticeable multiwavelength variability features that might resemble the behavior presented by eRASSt J0344-3327. In these sources, we can neither claim nor discard their TDE nature (see Table 4). For the remaining sources, the lack of TDE-like features in the multiwavelength data and the presence of hard X-rays disfavor the TDE scenario.

On the other hand, the longest repeating time detected for a QPE is 22 days (Guolo et al. 2024), which is not long enough to explain the long-term variability of our candidates, such as eRASSt J0530-4125 or eRASSt J1141+0635. Under the repeating transients framework, the sources with eROSITA-only X-ray data or those with short monitoring programs could belong to a very particular branch of the QPEs population. In this scenario, there would be an EMRI object orbiting the SMBH with long periods ( $\sim 1$  year), crossing the accretion disk in quasiregular intervals producing more energetic, harder, and long-lasting eruptions. Most of the sources in Table 4 are still marked as possible QPEs since this scenario is more complicated to prove or rule out with the available data. In case these sources are found to be QPEs, they would belong to an extreme class with one of the longest periods detected. This is assuming that there were no eruptions during the six months that eROSITA did not observe the source. Further X-ray observations with a higher cadence than eROSITA would provide better constraints on any plausible eruption timescales.

**SMBH binaries:** The variability landscape of the X-ray light curves presented in Figs. 7 and 8 is diverse and intricate. eRASSt J0530-4125 shows a smoother and recurrent quasiperiodic behavior with timescales on the order of one year. This object is interesting since AGNs with (quasi) periodic behavior are rare, especially in X-rays. D’Orazio & Charisi (2023) summarize the observational signatures of SMBHBs and provide a compilation of the known SMBHB candidates together with the techniques employed to select them.

Testing and confirming the binary nature of the best candidates is challenging and requires additional multiwavelength evidence. The last column in Table 4 lists the sources in which we have not discarded the SMBHB scenario based on their multiwavelength properties. We note that the X-ray periodic scenario needs further observational evidence with additional extended X-ray monitoring programs, complemented by optical and IR photometric data. Once the periodicity of the objects can be confirmed for several cycles, deep X-ray observations aiming to detect double-peaked Fe  $\text{K}\alpha$  emission line profiles will be needed to further test the SMBHB scenario.

### 6.3. Abundance of X-ray variable SMBHBs

Our aim in this work is to obtain an X-ray observational estimate of the fraction of extragalactic sources that could potentially host SMBHBs and we compare it to predictions. For this purpose, we need to compare the number of SMBHB candidates (Fig. 2) to the number of sources that could have been selected if they had met the specific variability criteria. This implies that not every

source in the eROSITA-De sky is bright enough to detect the specific variability pattern and thus search for SMBHB candidates.

We considered sources that are bright enough to have room for flux changes consistent with our selected sample. However, the exposure time across the sky is not uniform, leading to a nonuniform flux distribution. We note that 15 (out of 16) selected monitored sources in Fig. 2 have more than 50 counts in the bright state. Using this criterion, we found  $\sim 40,000$  sources among the 2.3 million sources that according to their *Gaia* properties and consistent with our selection criteria as set out in Sect. 2.2 are likely extragalactic and have at least one eROSITA scan with more than 50 detected counts. Thus, we estimated that one out of  $\sim 2600$  sources (a fraction of  $\sim 3.7 \times 10^{-4}$ ) has a  $F > 5$ , a  $S > 3$  and a flux in the bright state larger than  $\sim 5 \times 10^{-13} \text{ erg s}^{-1} \text{ cm}^{-2}$  (monitored sources in Fig. 2). This fraction corresponds to the most optimistic upper limit on the number of X-ray-selected sources. However, we also note that this calculation is limited by the cadence and scanning strategy of eROSITA.

Thus, we also had to obtain an estimate (under several assumptions) of the number of SMBHBs with all possible periods. We note that we are sensitive to windows of approximately one and two months around the tentative periods of  $\sim 4$  and  $\sim 12$  months, respectively. Sources whose tentative periods do not perfectly match the eROSITA cadence will show a larger discrepancy between the flux values of the corresponding bright or faint state, translating into smaller significances and factors in our selection criteria. Therefore, we consider this time window of  $\sim 3$  months (two months from the sources with periods  $\sim 12$  months and one from sources with periods of  $\sim 4$  months) as our eROSITA-sensitive time window.

According to theoretical models, when the separation of the SMBHBs in a binary system is on the order of the BLR size, the BLR starts suffering truncation (Popović 2012; De Rosa et al. 2019). We assume that at smaller separations, the SMBHBs are already embedded in the circumbinary disk, giving us a typical separation value for SMBHBs that could be emitting periodic X-ray emission. We find a BLR size of  $\sim 0.01$  pc (12 lt-days) following the BLR luminosity-size relation from Greene et al. (2010). Here, we have assumed an average total SMBHB mass of our sample of  $\sim 10^7 M_\odot$ , an average X-ray flux of  $\sim 7 \times 10^{-13} \text{ erg s}^{-1} \text{ cm}^{-2}$  in the eROSITA 0.2–2.3 keV band, an average X-ray luminosity in the 2–10 keV band of  $\sim 9.4 \times 10^{42} \text{ erg s}^{-1}$ , and an average redshift of  $z = 0.075$ . These are typical values obtained for our primary SMBHB sample (see, Sect. 5).

Binaries with these separations of 0.01 pc have periods of  $\sim 30$  years, assuming Keplerian motion, an equal mass ratio, and circular orbits. Assuming also that SMBHBs have a uniform distribution of orbital periods over these 30 years, we notice that the scanning pattern of eROSITA is only sensitive to three out of these 360 months, corresponding to a fraction of  $8 \times 10^{-3}$  (based on an average total SMBHB mass of  $\sim 10^7 M_\odot$ ). Therefore, combining these fractions, we estimate an upper limit on the probability of detecting X-ray variable SMBHBs of  $\sim 0.05$  when we consider the 15 sources of Fig. 2. This fraction will likely decrease when we account for the real origin of the sources and the false positive rate of the red-noise-induced variability in AGNs.

Theoretical and observational studies have predicted an abundance of SMBHBs based on several assumptions, selections, and techniques. Volonteri et al. (2009) predicted  $\sim 0.01 \text{ deg}^{-2}$  sub-pc binary quasars at  $z < 0.7$  based on the hierarchical assembly, growth, and dynamics of SMBHBs in a  $\Lambda$ CDM cosmology. This result corresponds to a fraction of  $\sim 6 \times 10^{-4}$

SMBHBs in their volume and flux-limited theoretical sample. Another study predicts an apparent occurrence of  $\sim 10\%$  sub-pc SMBHBs in SDSS based on bulk radial velocity shifts of the broad emission lines (Guo et al. 2019). Hayasaki et al. (2010) found that  $\sim 1\%$  of AGNs have close binary massive black holes with an orbital period of less than ten years based on the SMBH mass function and the theory of evolution of SMBHBs interacting with a circumbinary disk. Using a combination of cosmological, hydrodynamic simulations, binary merger models, and AGN spectra and variability prescriptions, Kelley et al. (2019) found that the expected fraction of SMBHB is  $\sim 1\%$  at  $z < 0.6$ . However, only a few (fractions about  $10^{-7}$ – $10^{-5}$ ) can be identifiable in the Catalina survey (CRTS) or LSST. From an observational point of view, Chen et al. (2020) found  $\sim 1$  quasar per  $\text{deg}^2$  with likely periodicity in their optical light curves in the overlapping region of the Dark Energy Survey Supernova (DES-SN) fields and the Sloan Digital Sky Survey Stripe 82 (SDSS-S82).

Although several assumptions were made, our optimistic observational probability of  $\sim 5\%$  is fully consistent with theoretical predictions and previous observational estimates. Longer X-ray monitoring campaigns might reduce the number of possible SMBHB candidates in this sample, thus reducing the currently derived observational probability.

#### 6.4. Gravitational waves expectations

In their latest stages, SMBHBs will lose most of their angular momentum due to GW production. Therefore, if our sources are the progenitors of such close GW-emitting SMBHBs, they will also be ideal targets of GW missions and their multiwavelength follow-up. The predictions from both methods would then be expected to be consistent with each other. However, we note that our X-ray-selected SMBHB candidates are only a subsample of the GW-SMBHB sample, as our objects need to be accreting to see their X-ray emission. Gravitational-wave missions, on the other hand, will also be sensitive to nonaccreting SMBHBs.

In principle, SMBHBs with masses calculated in our sample ( $\sim 10^7 M_\odot$ ) are detectable by space-borne interferometer GW missions such as the Laser Interferometer Space Antenna (LISA; Amaro-Seoane et al. 2017) or TianQin (Luo et al. 2016). However, the tentative orbital periods of our candidates are longer than those that will be probed by these missions.

Following Peters & Mathews (1963) and Peters (1964), we derive a GW-driven merging timescale for eRASSt J0530-4125 of  $4 \times 10^6$  years by assuming that the X-ray emission is effectively coming from a SMBHB in a GW-driven regime with circular orbits, a distance between the SMBHBs of 1.2 milli-pc, and a total mass of  $M_{H\beta} = 10^{7.23} M_\odot$  with equal mass ratios. In general, this GW-driven decay is faster for eccentric binaries but slower for binaries of unequal mass.

## 7. Conclusions

We have explored the largest time-domain X-ray catalog, searching for quasiperiodic light curves in extragalactic X-ray sources, aiming to discover a hidden population of SMBHB binaries. Using the *SRG/eROSITA* X-ray catalog of the Western Galactic hemisphere, we selected X-ray sources with “up-down-up-down” or “down-up-down-up” profiles (from eRASS scan to scan) in their 0.2–2.3 keV flux light curves.

Initially, we selected a total of 16 SMBHB candidates. Optical spectroscopic analysis confirmed the extragalactic and nuclear nature of 15 out of the 16 candidates. We found that most of the sources host low single-epoch SMBH masses ( $\sim 10^7 M_\odot$ )

based on the width and luminosity of the broad Balmer lines. Most of the sources are characterized as AGN, given their location in the BPT diagnostic diagram. By using their optical redshifts, we derived the observed X-ray luminosities for the sources ranging between  $\sim 10^{40\text{--}43} \text{ erg s}^{-1}$  in the 0.2–2.3 keV band. We claim that their luminous X-ray emission is very likely to originate in the vicinity of the SMBHB at their centers, thus ruling out an off-nuclear origin.

Extensive *Swift*-XRT and *NICER* X-ray monitoring campaigns followed up the primary SMBHB candidates with a typical cadence of one month. Given the monitoring strategy and the number of data points in the light curves, we found support for a 12 month periodicity in the galaxy eRASSt J0530-4125 at redshift  $z = 0.076$ . Unlike the optical and IR emission, the UV bands of the *Swift*-UVOT light curves tend to follow the variability trend defined by the X-ray light curve with a tentative period of about one year. The lack of optical and IR variability is consistent with the scenario where the SMBHB is surrounded by a colder circumbinary disk that does not vary with the orbital period of the binary. Assuming that the periodic signal is caused by a SMBHB, we calculated a distance of 1.2 milli-pc between the orbiting SMBHBs. The optical spectral analysis of the source shows that eRASSt J0530-4125 has a galaxy-like spectrum with weak emission lines and a lack of strong broad emission lines, leading to an uncertain single-epoch SMBHB mass measurement of  $\log M_{\text{bh}}(\text{H}\beta)/M_\odot = 7.26 \pm 0.48$ . Based on the optical narrow emission lines, the gas in the host galaxy can be explained by an ionizing continuum from star-forming regions, rather than AGN emission. However, this does not explain the X-ray emission.

We emphasize that the effect of stochastic red-noise X-ray variability produced by accretion onto a single SMBHB can mimic a few cycles of periodic behavior, affecting and biasing our sample as well as our interpretation of the X-ray light curves (possibly including eRASSt J0530-4125). The effect of red-noise variability in our sample will be investigated in detail in the second paper of this program (Tubín-Arenas et al., in prep.). Simulations of stochastic AGN light curves coupled with an eROSITA-like observation pattern will provide a quantifiable estimation of the false positives in our sample and will help us improve the source selection. However, longer and extended monitoring programs will also be needed to discriminate between the SMBHB scenario and red-noise-induced variability.

Under the assumption that stochastic red-noise effects do not drive the variability, we observed that our sources share features with some of the rarest transient events. We noted that repeating TDEs might potentially meet our initial eROSITA selection criteria. However, most of the sources in our sample exhibit X-rays consistent with AGN emission ( $\Gamma \sim 2$ ), and their multiwavelength properties do not indicate evidence of optical or IR flares. The absence of a multiwavelength response to the X-ray emission resembles the scenario recently unveiled by QPEs, where they are only detectable in the soft X-ray regime. Our sources, however, display harder X-ray emission with longer timescale variability. Therefore, our current multiwavelength data make it unlikely that for the majority of our sources a TDE and QPE scenario is the origin of the quasiperiodic light curve signature. The SMBHB scenario remains a likely origin for the X-ray emission.

The number of selected SMBHB candidates with quasiperiodic X-ray signals was used to derive an optimistic estimate of  $\sim 0.05$  SMBHB per X-ray emitting galaxy. This value is consistent with existing theoretical predictions that suggest that  $< 1\text{--}10\%$  of the galaxies host a SMBHB.

*SRG/eROSITA* is the first repeating all-sky X-ray survey that has opened a window to detect new and rare extragalactic events,

such as TDEs, QPEs, and SMBHBs. Combined with spectroscopic and multiwavelength follow-up studies, it is paving a new path toward finding and characterizing the demographics of SMBHBs. We have seen that multiwavelength monitoring programs covering multiple cycles are needed to fully test the scenarios proposed in this paper. Unfortunately, given the timescales displayed by the objects, X-ray programs are expensive and not always available. This highlights the need for missions such as *SRG/eROSITA* that were designed to perform all-sky monitoring of X-ray sources at regular intervals. Current and future X-ray missions will revolutionize the search for SMBHBs by observing the Fe  $K\alpha$  emission lines with unprecedented spectral resolution. In addition, *XRISM* (Tashiro et al. 2018) and *NewAthena* (Cruise et al. 2025) can and will provide high-throughput imaging with high X-ray spectral resolution down to  $\sim 5$  eV in the 0.3–12 keV band. High-resolution observations at these energies will easily resolve any double-peaked lines or other effects of the binary in the Fe  $K\alpha$  line profile (McKernan & Ford 2015).

**Acknowledgements.** We thank the referee for their useful comments that helped to improve the manuscript. D.T. acknowledges support by DLR grant FKZ 50 OR 2203. M.K. is supported by DLR grant FKZ 50 OR 2307. G.L. acknowledges support from the German DLR under contract 50 QR 2104. D.H. acknowledges support from DLR grant FKZ 50 OR 2003. AGM acknowledges support from Narodowe Centrum Nauki (NCN) grant 2018/31/G/ST9/03224, and partial support from NCN grant 2019/35/B/ST9/03944. This work is based on data from *eROSITA*, the soft X-ray instrument aboard *SRG*, a joint Russian-German science mission supported by the Russian Space Agency (Roscosmos), in the interests of the Russian Academy of Sciences represented by its Space Research Institute (IKI), and the Deutsches Zentrum für Luft- und Raumfahrt (DLR). The *SRG* spacecraft was built by Lavochkin Association (NPOL) and its subcontractors, and is operated by NPOL with support from the Max Planck Institute for Extraterrestrial Physics (MPE). The development and construction of the *eROSITA* X-ray instrument was led by MPE, with contributions from the Dr. Karl Remeis Observatory Bamberg & ECAP (FAU Erlangen-Nürnberg), the University of Hamburg Observatory, the Leibniz Institute for Astrophysics Potsdam (AIP), and the Institute for Astronomy and Astrophysics of the University of Tübingen, with the support of DLR and the Max Planck Society. The Argelander Institute for Astronomy of the University of Bonn and the Ludwig Maximilians Universität Munich also participated in the science preparation for *eROSITA*. The *eROSITA* data shown here were processed using the eSASS/NRTA software system developed by the German *eROSITA* consortium. This work made use of data supplied by the UK Swift Science Data Centre at the University of Leicester. We acknowledge the use of public data from the Swift data archive. Based on observations collected at the European Organisation for Astronomical Research in the Southern Hemisphere under ESO programme 112.263K. This paper uses observations made at the South African Astronomical Observatory (SAAO). This work has made use of data from the Asteroid Terrestrial-impact Last Alert System (ATLAS) project. The Asteroid Terrestrial-impact Last Alert System (ATLAS) project is primarily funded to search for near earth asteroids through NASA grants NN12AR55G, 80NSSC18K0284, and 80NSSC18K1575; byproducts of the NEO search include images and catalogs from the survey area. This work was partially funded by Kepler/K2 grant J1944/80NSSC19K0112 and HST GO-15889, and STFC grants ST/T000198/1 and ST/S006109/1. The ATLAS science products have been made possible through the contributions of the University of Hawaii Institute for Astronomy, the Queen’s University Belfast, the Space Telescope Science Institute, the South African Astronomical Observatory, and The Millennium Institute of Astrophysics (MAS), Chile. The Legacy Surveys consist of three individual and complementary projects: the Dark Energy Camera Legacy Survey (DECaLS; Proposal ID #2014B-0404; PIs: David Schlegel and Arjun Dey), the Beijing-Arizona Sky Survey (BASS; NOAO Prop. ID #2015A-0801; PIs: Zhou Xu and Xiaohui Fan), and the Mayall z-band Legacy Survey (MzLS; Prop. ID #2016A-0453; PI: Arjun Dey). DECaLS, BASS and MzLS together include data obtained, respectively, at the Blanco telescope, Cerro Tololo Inter-American Observatory, NSF’s NOIRLab; the Bok telescope, Steward Observatory, University of Arizona; and the Mayall telescope, Kitt Peak National Observatory, NOIRLab. Pipeline processing and analyses of the data were supported by NOIRLab and the Lawrence Berkeley National Laboratory (LBNL). The Legacy Surveys project is honored to be permitted to conduct astronomical research on Iolkam Du’ag (Kitt Peak), a mountain with particular significance to the Tohono O’odham Nation. NOIRLab is operated by the Association of Universities for Research in Astronomy (AURA) under a coop-

erative agreement with the National Science Foundation. LBNL is managed by the Regents of the University of California under contract to the U.S. Department of Energy. This project used data obtained with the Dark Energy Camera (DECam), which was constructed by the Dark Energy Survey (DES) collaboration. Funding for the DES Projects has been provided by the U.S. Department of Energy, the U.S. National Science Foundation, the Ministry of Science and Education of Spain, the Science and Technology Facilities Council of the United Kingdom, the Higher Education Funding Council for England, the National Center for Supercomputing Applications at the University of Illinois at Urbana-Champaign, the Kavli Institute of Cosmological Physics at the University of Chicago, Center for Cosmology and Astro-Particle Physics at the Ohio State University, the Mitchell Institute for Fundamental Physics and Astronomy at Texas A&M University, Financiadora de Estudos e Projetos, Fundação Carlos Chagas Filho de Amparo, Financiadora de Estudos e Projetos, Fundação Carlos Chagas Filho de Amparo a Pesquisa do Estado do Rio de Janeiro, Conselho Nacional de Desenvolvimento Científico e Tecnológico and the Ministério da Ciência, Tecnologia e Inovação, the Deutsche Forschungsgemeinschaft and the Collaborating Institutions in the Dark Energy Survey. The Collaborating Institutions are Argonne National Laboratory, the University of California at Santa Cruz, the University of Cambridge, Centro de Investigaciones Energeticas, Medioambientales y Tecnologicas-Madrid, the University of Chicago, University College London, the DES-Brazil Consortium, the University of Edinburgh, the Eidgenössische Technische Hochschule (ETH) Zurich, Fermi National Accelerator Laboratory, the University of Illinois at Urbana-Champaign, the Institut de Ciències de l’Espai (IEEC/CSIC), the Institut de Física d’Altes Energies, Lawrence Berkeley National Laboratory, the Ludwig-Maximilians-Universität München and the associated Excellence Cluster Universe, the University of Michigan, NSF’s NOIRLab, the University of Nottingham, the Ohio State University, the University of Pennsylvania, the University of Portsmouth, SLAC National Accelerator Laboratory, Stanford University, the University of Sussex, and Texas A&M University. BASS is a key project of the Telescope Access Program (TAP), which has been funded by the National Astronomical Observatories of China, the Chinese Academy of Sciences (the Strategic Priority Research Program “The Emergence of Cosmological Structures” Grant # XDB09000000), and the Special Fund for Astronomy from the Ministry of Finance. The BASS is also supported by the External Cooperation Program of Chinese Academy of Sciences (Grant # 114A11KYSB20160057), and Chinese National Natural Science Foundation (Grant # 12120101003, # 11433005). The Legacy Survey team makes use of data products from the Near-Earth Object Wide-field Infrared Survey Explorer (NEOWISE), which is a project of the Jet Propulsion Laboratory/California Institute of Technology. NEOWISE is funded by the National Aeronautics and Space Administration. The Legacy Surveys imaging of the DESI footprint is supported by the Director, Office of Science, Office of High Energy Physics of the U.S. Department of Energy under Contract No. DE-AC02-05CH1123, by the National Energy Research Scientific Computing Center, a DOE Office of Science User Facility under the same contract; and by the U.S. National Science Foundation, Division of Astronomical Sciences under Contract No. AST-0950945 to NOAO.

## References

- Agazie, G., Anumarlapudi, A., Archibald, A. M., et al. 2023, *ApJ*, 951, L50  
 Amaro-Seoane, P., Audley, H., Babak, S., et al. 2017, arXiv e-prints [arXiv:1702.00786]  
 Arcodia, R., Merloni, A., Nandra, K., et al. 2021, *Nature*, 592, 704  
 Arcodia, R., Liu, Z., Merloni, A., et al. 2024, *A&A*, 684, A64  
 Arnaud, K. A. 1996, in Astronomical Data Analysis Software and Systems V, eds. G. H. Jacoby, & J. Barnes, *Astronomical Society of the Pacific Conference Series*, 101, 17  
 Baldwin, J. A., Phillips, M. M., & Terlevich, R. 1981, *PASP*, 93, 5  
 Begelman, M. C., Blandford, R. D., & Rees, M. J. 1980, *Nature*, 287, 307  
 Bogdanović, T., Miller, M. C., & Blecha, L. 2022, *Liv. Rev. Relat.*, 25, 3  
 Bon, E., Jovanović, P., Marziani, P., et al. 2012, *ApJ*, 759, 118  
 Bowen, D. B., Mewes, V., Campanelli, M., et al. 2018, *ApJ*, 853, L17  
 Bowen, D. B., Mewes, V., Noble, S. C., et al. 2019, *ApJ*, 879, 76  
 Brunner, H., Liu, T., Lamer, G., et al. 2022, *A&A*, 661, A1  
 Cappellari, M. 2017, *MNRAS*, 466, 798  
 Cappellari, M. 2023, *MNRAS*, 526, 3273  
 Cappellari, M., & Emsellem, E. 2004, *PASP*, 116, 138  
 Caproni, A., Abraham, Z., & Monteiro, H. 2013, *MNRAS*, 428, 280  
 Cash, W. 1979, *ApJ*, 228, 939  
 Chandrasekhar, S. 1943, *ApJ*, 97, 255  
 Charisi, M., Bartos, I., Haiman, Z., et al. 2016, *MNRAS*, 463, 2145  
 Charisi, M., Haiman, Z., Schiminovich, D., & D’Orazio, D. J. 2018, *MNRAS*, 476, 4617  
 Chen, Y.-C., Liu, X., Liao, W.-T., et al. 2020, *MNRAS*, 499, 2245  
 Cruise, L. A., Gilbank, D., van Gend, C., et al. 2019, *J. Astron. Telesc. Instrum. Syst.*, 5, 024007

- Cruise, M., Guainazzi, M., Aird, J., et al. 2025, *Nat. Astron.*, **9**, 36
- d'Ascoli, S., Noble, S. C., Bowen, D. B., et al. 2018, *ApJ*, **865**, 140
- de la Parra, P. V., Kiehlmann, S., Mroz, P., et al. 2024, arxiv e-prints [arxiv:2408.02645v1]
- De Rosa, A., Vignali, C., Bogdanović, T., et al. 2019, *New Astron. Rev.*, **86**, 101525
- De Rosa, A., Vignali, C., Severgnini, P., et al. 2023, *MNRAS*, **519**, 5149
- Dey, L., Gopakumar, A., Valtonen, M., et al. 2019a, *Universe*, **5**, 108
- Dey, A., Schlegel, D. J., Lang, D., et al. 2019b, *ApJ*, **157**, 168
- Doan, A., Eracleous, M., Runnoe, J. C., et al. 2020, *MNRAS*, **491**, 1104
- D'Orazio, D. J., & Charisi, M. 2023, arXiv e-prints [arXiv:2310.16896]
- D'Orazio, D. J., & Di Stefano, R. 2018, *MNRAS*, **474**, 2975
- D'Orazio, D. J., Haiman, Z., & MacFadyen, A. 2013, *MNRAS*, **436**, 2997
- D'Orazio, D. J., Haiman, Z., & Schiminovich, D. 2015, *Nature*, **525**, 351
- Dressler, A., Bigelow, B., Hare, T., et al. 2011, *PASP*, **123**, 288
- EPTA Collaboration (InPTA Collaboration, et al.) 2023, *A&A*, **678**, A50
- EPTA Collaboration (InPTA Collaboration, et al.) 2024, *A&A*, **685**, A94
- Eracleous, M., & Halpern, J. P. 1994, *ApJS*, **90**, 1
- Eracleous, M., Lewis, K. T., & Flohic, H. M. L. G. 2009, *New Astron. Rev.*, **53**, 133
- Eracleous, M., Boroson, T. A., Halpern, J. P., & Liu, J. 2012, *ApJS*, **201**, 23
- Escala, A., Larson, R. B., Coppi, P. S., & Mardones, D. 2005, *ApJ*, **630**, 152
- Evans, P. A., Beardmore, A. P., Page, K. L., et al. 2007, *A&A*, **469**, 379
- Evans, P. A., Beardmore, A. P., Page, K. L., et al. 2009, *MNRAS*, **397**, 1177
- Evans, P. A., Osborne, J. P., Beardmore, A. P., et al. 2014, *ApJS*, **210**, 8
- Evans, P. A., Page, K. L., Osborne, J. P., et al. 2020, *ApJS*, **247**, 54
- Evans, P. A., Page, K. L., Beardmore, A. P., et al. 2023, *MNRAS*, **518**, 174
- Farrell, S. A., Webb, N. A., Barret, D., Godet, O., & Rodrigues, J. M. 2009, *Nature*, **460**, 73
- Farris, B. D., Duffell, P., MacFadyen, A. I., & Haiman, Z. 2014, *ApJ*, **783**, 134
- Farris, B. D., Duffell, P., MacFadyen, A. I., & Haiman, Z. 2015, *MNRAS*, **446**, L36
- Freudling, W., Romaniello, M., Bramich, D. M., et al. 2013, *A&A*, **559**, A96
- Gaia Collaboration (Brown, A. G. A., et al.) 2021, *A&A*, **649**, A1
- Gehrels, N., Chincarini, G., Giommi, P., et al. 2004, *ApJ*, **611**, 1005
- Gezari, S. 2021, *ARA&A*, **59**, 21
- Ginsburg, A., & Mirocha, J. 2011, Astrophysics Source Code Library [record ascl:1109.001]
- Giustini, M., Miniutti, G., & Saxton, R. D. 2020, *A&A*, **636**, L2
- Goad, M. R., Tyler, L. G., Beardmore, A. P., et al. 2007, *A&A*, **476**, 1401
- Gong, H., Liu, J., & Maccarone, T. 2016, *ApJS*, **222**, 12
- Graham, M. J., Djorgovski, S. G., Stern, D., et al. 2015, *MNRAS*, **453**, 1562
- Greene, J. E., Hood, C. E., Barth, A. J., et al. 2010, *ApJ*, **723**, 409
- Grotto, I., Rau, A., Salvato, M., et al. 2025, *A&A*, **693**, A62
- Gültekin, K., & Miller, J. M. 2012, *ApJ*, **761**, 90
- Guo, H., Liu, X., Shen, Y., et al. 2019, *MNRAS*, **482**, 3288
- Guolo, M., Pasham, D. R., Zajaček, M., et al. 2024, *Nat. Astron.*, **8**, 347
- Haiman, Z. 2017, *Phys. Rev. D*, **96**, 023004
- Hayasaki, K., Mineshige, S., & Sudou, H. 2007, *PASJ*, **59**, 427
- Hayasaki, K., Mineshige, S., & Ho, L. C. 2008, *ApJ*, **682**, 1134
- Hayasaki, K., Ueda, Y., & Isobe, N. 2010, *PASJ*, **62**, 1351
- HI4PI Collaboration (Ben Bekhti, N., et al.) 2016, *A&A*, **594**, A116
- Hills, J. G. 1975, *Nature*, **254**, 295
- Hinshaw, G., Weiland, J. L., Hill, R. S., et al. 2009, *ApJS*, **180**, 225
- Holgado, A. M., Sesana, A., Sandrinelli, A., et al. 2018, *MNRAS*, **481**, L74
- Jansen, F., Lumb, D., Altieri, B., et al. 2001, *A&A*, **365**, L1
- Jones, D. H., Saunders, W., Colless, M., et al. 2004, *MNRAS*, **355**, 747
- Jones, D. H., Read, M. A., Saunders, W., et al. 2009, *MNRAS*, **399**, 683
- Jovanović, P., Borka Jovanović, V., Borka, D., & Bogdanović, T. 2014, *Adv. Space Res.*, **54**, 1448
- Jovanović, P., Borka Jovanović, V., Borka, D., & Popović, L. Č. 2020, *Contrib. Astron. Obs. Skalnate Pleso*, **50**, 219
- Jovanović, P., Simić, S., Borka Jovanović, V., Borka, D., & Popović, L. Č. 2025, *Adv. Space Res.*, **75**, 1441
- Kaaret, P., Feng, H., & Roberts, T. P. 2017, *ARA&A*, **55**, 303
- Kahabka, P., Puzia, T. H., & Pietsch, W. 2000, *A&A*, **361**, 491
- Kauffmann, G., Heckman, T. M., Tremonti, C., et al. 2003, *MNRAS*, **346**, 1055
- Kelley, L. Z., Haiman, Z., Sesana, A., & Hernquist, L. 2019, *MNRAS*, **485**, 1579
- Kewley, L. J., Heisler, C. A., Dopita, M. A., et al. 2000, *ApJ*, **530**, 704
- Kewley, L. J., Dopita, M. A., Sutherland, R. S., Heisler, C. A., & Trevena, J. 2001, *ApJ*, **556**, 121
- Kewley, L. J., Groves, B., Kauffmann, G., & Heckman, T. 2006, *MNRAS*, **372**, 961
- Kiehlmann, S., Parra, P. V. D. L., Sullivan, A., et al. 2024, *ApJ*, accepted [arxiv:2407.09647v1]
- King, O. G., Hovatta, T., Max-Moerbeck, W., et al. 2013, *MNRAS*, **436**, L114
- Kollatschny, W., Weilbacher, P. M., Ochmann, M. W., et al. 2020, *A&A*, **633**, A79
- Komossa, S., Grupe, D., Gallo, L. C., et al. 2021a, *ApJ*, **923**, 51
- Komossa, S., Grupe, D., Kraus, A., et al. 2021b, *Universe*, **7**, 261
- Koss, M., Mushotzky, R., Treister, E., et al. 2012, *ApJ*, **746**, L22
- Koss, M. J., Blecha, L., Bernhard, P., et al. 2018, *Nature*, **563**, 214
- Krishnan, S., Markowitz, A. G., Schwarzenberg-Czerny, A., & Middleton, M. J. 2021, *MNRAS*, **508**, 3975
- Lasker, B. M., Doggett, J., McLean, B., et al. 1996, in *Astronomical Data Analysis Software and Systems V*, eds. G. H. Jacoby, & J. Barnes, *Astronomical Society of the Pacific Conference Series*, **101**, 88
- Lasota, J. P., Alexander, T., Dubus, G., et al. 2011, *ApJ*, **735**, 89
- Lawrence, A., Watson, M. G., Pounds, K. A., & Elvis, M. 1987, *Nature*, **325**, 694
- Linial, I., & Metzger, B. D. 2023, *ApJ*, **957**, 34
- Liska, M., Hesp, C., Tchekhovskoy, A., et al. 2018, *MNRAS*, **474**, L81
- Liu, X., Shen, Y., Bian, F., Loeb, A., & Tremaine, S. 2014, *ApJ*, **789**, 140
- Liu, T., Gezari, S., Burgett, W., et al. 2016a, *ApJ*, **833**, 6
- Liu, T., Eracleous, M., & Halpern, J. P. 2016b, *ApJ*, **817**, 42
- Liu, T., Gezari, S., & Miller, M. C. 2018, *ApJ*, **859**, L12
- Liu, T., Koss, M., Blecha, L., et al. 2020, *ApJ*, **896**, 122
- Liu, Z., Malyali, A., Krumpe, M., et al. 2023, *A&A*, **669**, A75
- Liu, Z., Ryu, T., Goodwin, A. J., et al. 2024, *A&A*, **683**, L13
- Lodato, G., Nayakshin, S., King, A. R., & Pringle, J. E. 2009, *MNRAS*, **398**, 1392
- Lomb, N. R. 1976, *Ap&SS*, **39**, 447
- Luo, J., Chen, L.-S., Duan, H.-Z., et al. 2016, *Class. Quant. Grav.*, **33**, 035010
- Luo, D., Jiang, N., & Liu, X. 2025, *ApJ*, **978**, 86
- MacFadyen, A. I., & Milosavljević, M. 2008, *ApJ*, **672**, 83
- MacLeod, C. L., Ivezić, Ž., Kochanek, C. S., et al. 2010, *ApJ*, **721**, 1014
- Mainzer, A., Bauer, J., Cutri, R. M., et al. 2014, *ApJ*, **792**, 30
- Malyali, A., Liu, Z., Rau, A., et al. 2023, *MNRAS*, **520**, 3549
- Markowitz, A., Edelson, R., Vaughan, S., et al. 2003, *ApJ*, **593**, 96
- Masci, F. J., Laher, R. R., Rusholme, B., et al. 2018, *PASP*, **131**, 018003
- McHardy, I., & Czerny, B. 1987, *Nature*, **325**, 696
- McHardy, I. M., Koerding, E., Knigge, C., Uttley, P., & Fender, R. P. 2006, *Nature*, **444**, 730
- McKernan, B., & Ford, K. E. S. 2015, *MNRAS*, **452**, L1
- McKernan, B., Ford, K. E. S., Kocsis, B., & Haiman, Z. 2013, *MNRAS*, **432**, 1468
- Meisner, A. M., Caselden, D., Schlafly, E. F., & Kiwy, F. 2023, *AJ*, **165**, 36
- Mejía-Restrepo, J. E., Trakhtenbrot, B., Koss, M. J., et al. 2022, *ApJS*, **261**, 5
- Merloni, A., Predehl, P., Becker, W., et al. 2012, arXiv e-prints [arXiv:1209.3114]
- Merloni, A., Lamer, G., Liu, T., et al. 2024, *A&A*, **682**, A34
- Milosavljević, M., & Merritt, D. 2003, *ApJ*, **596**, 860
- Miniutti, G., Saxton, R. D., Giustini, M., et al. 2019, *Nature*, **573**, 381
- Miniutti, G., Giustini, M., Arcodia, R., et al. 2023, *A&A*, **670**, A93
- Mirza, M. A., Tahir, A., Khan, F. M., et al. 2017, *MNRAS*, **470**, 940
- Nicholl, M., Pasham, D. R., Mummary, A., et al. 2024, *Nature*, **634**, 804
- Noble, S. C., Mundim, B. C., Nakano, H., et al. 2012, *ApJ*, **755**, 51
- O'Neill, S., Kiehlmann, S., Readhead, A. C. S., et al. 2022, *ApJ*, **926**, L35
- Osterbrock, D. E., & Ferland, G. J. 2006, *Astrophysics of Gaseous Nebulae and Active Galactic Nuclei*, 2nd edn. (Sausalito, CA: University Science Books)
- Pan, X., Li, S.-L., Cao, X., Miniutti, G., & Gu, M. 2022, *ApJ*, **928**, L18
- Paolillo, M., Papadakis, I. E., Brandt, W. N., et al. 2023, *A&A*, **673**, A68
- Pasham, D., Coughlin, E., Nixon, C., et al. 2024, *ApJ*, submitted [arXiv:2411.05948]
- Payne, A. V., Shappee, B. J., Hinkle, J. T., et al. 2021, *ApJ*, **910**, 125
- Peters, P. C. 1964, *Phys. Rev.*, **136**, B1224
- Peters, P. C., & Mathews, J. 1963, *Phys. Rev.*, **131**, 435
- Pogge, R. W., Atwood, B., Brewer, D. F., et al. 2010, in *Ground-based and Airborne Instrumentation for Astronomy III*, eds. I. S. McLean, S. K. Ramsay, & H. Takami, *Society of Photo-Optical Instrumentation Engineers (SPIE) Conference Series*, **7735**, 77350A
- Popović, L. Č. 2012, *New Astron. Rev.*, **56**, 74
- Predehl, P., Andritschke, R., Arefiev, V., et al. 2021, *A&A*, **647**, A1
- Press, W. H. 1978, *Comm. Astrophys.*, **7**, 103
- Quintin, E., Webb, N. A., Guillot, S., et al. 2023, *A&A*, **675**, A152
- Reardon, D. J., Zic, A., Shannon, R. M., et al. 2023, *ApJ*, **951**, L6
- Rees, M. J. 1988, *Nature*, **333**, 523
- Ren, G.-W., Ding, N., Zhang, X., et al. 2021, *MNRAS*, **506**, 3791
- Ricci, C., Bauer, F. E., Treister, E., et al. 2017, *MNRAS*, **468**, 1273
- Roedig, C., Krolík, J. H., & Miller, M. C. 2014, *ApJ*, **785**, 115
- Roming, P. W. A., Kennedy, T. E., Mason, K. O., et al. 2005, *Space Sci. Rev.*, **120**, 95
- Runnoe, J. C., Eracleous, M., Pennell, A., et al. 2017, *MNRAS*, **468**, 1683
- Ryu, T., Perna, R., Haiman, Z., Ostriker, J. P., & Stone, N. C. 2018, *MNRAS*, **473**, 3410

- Saxton, R., Komossa, S., Auchettl, K., & Jonker, P. G. 2020, *Space Sci. Rev.*, **216**, 85
- Scargle, J. D. 1982, *ApJ*, **263**, 835
- Schawinski, K., Thomas, D., Sarzi, M., et al. 2007, *MNRAS*, **382**, 1415
- Serafinelli, R., Severgnini, P., Braito, V., et al. 2020, *ApJ*, **902**, 10
- Servillat, M., Farrell, S. A., Lin, D., et al. 2011, *ApJ*, **743**, 6
- Sesana, A., Roedig, C., Reynolds, M. T., & Dotti, M. 2012, *MNRAS*, **420**, 860
- Severgnini, P., Cicone, C., Della Ceca, R., et al. 2018, *MNRAS*, **479**, 3804
- Shen, Y., Liu, X., Loeb, A., & Tremaine, S. 2013, *ApJ*, **775**, 49
- Shingles, L., Smith, K. W., Young, D. R., et al. 2021, *TNSAN*, **7**, 1
- Shu, X., Zhang, W., Li, S., et al. 2020, *Nat. Commun.*, **11**, 5876
- Sillanpää, A., Haarala, S., Valtonen, M. J., Sundelius, B., & Byrd, G. G. 1988, *ApJ*, **325**, 628
- Smith, K. W., Smartt, S. J., Young, D. R., et al. 2020, *PASP*, **132**, 085002
- Storchi-Bergmann, T., Schimoia, J. S., Peterson, B. M., et al. 2017, *ApJ*, **835**, 236
- Suková, P., Tombesi, F., Pasham, D. R., et al. 2024, arXiv e-prints [arXiv:2411.04592]
- Sunyaev, R., Arefiev, V., Babyshkin, V., et al. 2021, *A&A*, **656**, A132
- Tanaka, T., Menou, K., & Haiman, Z. 2012, *MNRAS*, **420**, 705
- Tang, Y., Haiman, Z., & MacFadyen, A. 2018, *MNRAS*, **476**, 2249
- Tashiro, M., Maejima, H., Toda, K., et al. 2018, in *Space Telescopes and Instrumentation 2018: Ultraviolet to Gamma Ray*, eds. J. W. A. den Herder, S. Nikzad, & K. Nakazawa, *International Society for Optics and Photonics (SPIE)*, **10699**, 1069922
- Terwel, J. H., & Jonker, P. G. 2022, *MNRAS*, **512**, L80
- Tody, D. 1986, in *Instrumentation in Astronomy VI*, ed. D. L. Crawford, *Society of Photo-Optical Instrumentation Engineers (SPIE) Conference Series*, **627**, 733
- Tony, J. L., Denneau, L., Heinze, A. N., et al. 2018, *PASP*, **130**, 064505
- Treister, E., Privon, G. C., Sartori, L. F., et al. 2018, *ApJ*, **854**, 83
- Tsalmantza, P., Decarli, R., Dotti, M., & Hogg, D. W. 2011, *ApJ*, **738**, 20
- Tubín, D., Treister, E., D’Ago, G., et al. 2021, *ApJ*, **911**, 100
- Tubín-Arenas, D., Krumpe, M., Lamer, G., et al. 2024, *A&A*, **682**, A35
- Vasiliev, E., Antonini, F., & Merritt, D. 2014, *ApJ*, **785**, 163
- Vaughan, S. 2005, *A&A*, **431**, 391
- Vaughan, S., Edelson, R., Warwick, R. S., & Uttley, P. 2003, *MNRAS*, **345**, 1271
- Vaughan, S., Uttley, P., Markowitz, A. G., et al. 2016, *MNRAS*, **461**, 3145
- Vazdekis, A., Koleva, M., Ricciardelli, E., Röck, B., & Falcón-Barroso, J. 2016, *MNRAS*, **463**, 3409
- Veilleux, S., & Osterbrock, D. E. 1987, *ApJS*, **63**, 295
- Verner, D. A., Ferland, G. J., Korista, K. T., & Yakovlev, D. G. 1996, *ApJ*, **465**, 487
- Vestergaard, M., & Peterson, B. M. 2006, *ApJ*, **641**, 689
- Volonteri, M., Miller, J. M., & Dotti, M. 2009, *ApJ*, **703**, L86
- Wang, L., Greene, J. E., Ju, W., et al. 2017, *ApJ*, **834**, 129
- Wang, J.-M., Songsheng, Y.-Y., Li, Y.-R., & Du, P. 2023, *MNRAS*, **518**, 3397
- Webb, N., Cseh, D., Lenc, E., et al. 2012, *Science*, **337**, 554
- Wenger, M., Ochsenbein, F., Egret, D., et al. 2000, *A&AS*, **143**, 9
- Westernacher-Schneider, J. R., Zrake, J., MacFadyen, A., & Haiman, Z. 2022, *Phys. Rev. D*, **106**, 103010
- Wevers, T., Pasham, D. R., Jalan, P., Rakshit, S., & Arcodia, R. 2022, *A&A*, **659**, L2
- Wevers, T., French, K. D., Zabludoff, A. I., et al. 2024, *ApJ*, **970**, L23
- White, S. D. M., & Frenk, C. S. 1991, *ApJ*, **379**, 52
- White, S. D. M., & Rees, M. J. 1978, *MNRAS*, **183**, 341
- Wilms, J., Allen, A., & McCray, R. 2000, *ApJ*, **542**, 914
- Witt, C. A., Charisi, M., Taylor, S. R., & Burke-Spolaor, S. 2022, *ApJ*, **936**, 89
- Wright, E. L., Eisenhardt, P. R. M., Mainzer, A. K., et al. 2010, *AJ*, **140**, 1868
- Xian, J., Zhang, F., Dou, L., He, J., & Shu, X. 2021, *ApJ*, **921**, L32
- Xu, H., Chen, S., Guo, Y., et al. 2023, *Res. Astron. Astrophys.*, **23**, 075024

## Appendix A: Individual properties of the SMBHB candidates

### A.1. eRASSt J0344-3327

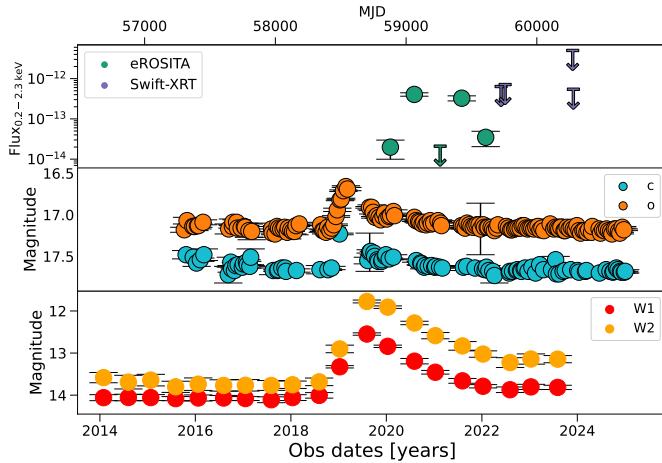


**Fig. A.1.** Multiwavelength light curve of eRASSt J0344-3327. X-ray data is given by *SRG/eROSITA* (green markers) and *Swift-XRT* (purple upper limits) in the top panel. Optical data is retrieved from ATLAS in their "c" and "o" bands (light-blue and orange markers) and presented in bins of 15 days in the middle panel. The WISE light curve (red and yellow markers) is shown in the bottom panel.

eRASSt J0344-3327 ( $z = 0.09$ ) is the source showing the largest flux ratio between the bright and faint states of the eROSITA light curve. The source is a galaxy with AGN features, given the relatively strong  $[\text{O III}]\lambda 5007\text{\AA}$  line and the BPT diagram.

eRASSt J0344-3327 was observed four times by *Swift-XRT* between 2022-05-05 and 2023-11-09, and no X-ray source was detected at the position of eRASSt J0344-3327. The *Swift-XRT* LSXPS Upper limit server reports a  $3\sigma$  upper limit of  $2.0 \times 10^{-3}$  cts  $\text{s}^{-1}$  in the 0.3–10.0 keV stacked image that corresponds with a  $3\sigma$  upper flux limit of  $1.8 \times 10^{-13}$  erg  $\text{s}^{-1}$   $\text{cm}^{-2}$  assuming a Galactic-absorbed power-law spectral model with a column density and photon index given by the values in Table 3 ( $n_{\text{H}} = 1.57 \times 10^{20}$  cm $^{-2}$ ;  $\Gamma = 5.35$ ). Assuming this Galactic-absorbed power-law spectral model, we scaled the 0.3–10.0 keV upper limit flux to the *SRG/eROSITA* energy bands, as shown in Fig. 7. We note that the *Swift-XRT* upper limits of 2022 are still consistent with the periodic prediction. However, deeper observations are needed to confirm or rule out any possible rebrightening expected from our SMBHB predictions.

*NICER* observed the galaxy between July and October 2022. The stacked observations have a net exposure time of 16 ks. The spectral fitting shows that it is a soft source ( $\Gamma \sim 5$ ) that can also be characterized by an accretion disk consisting of multiple blackbody components ( $kT \sim 70$  eV).

ATLAS and WISE light curves in Fig. A.1 show a sharp brightening between August 2018 and January 2019 and reached its peak in August 2019 according to the WISE data. The optical and IR fluxes have decayed exponentially since then. This behavior suggests a tidal disruption event (TDE, Hills 1975; Rees 1988) where the soft X-ray emission seen by *SRG/eROSITA* is likely produced by the repeated accretion of the debris material onto the SMBH after the disruption event.

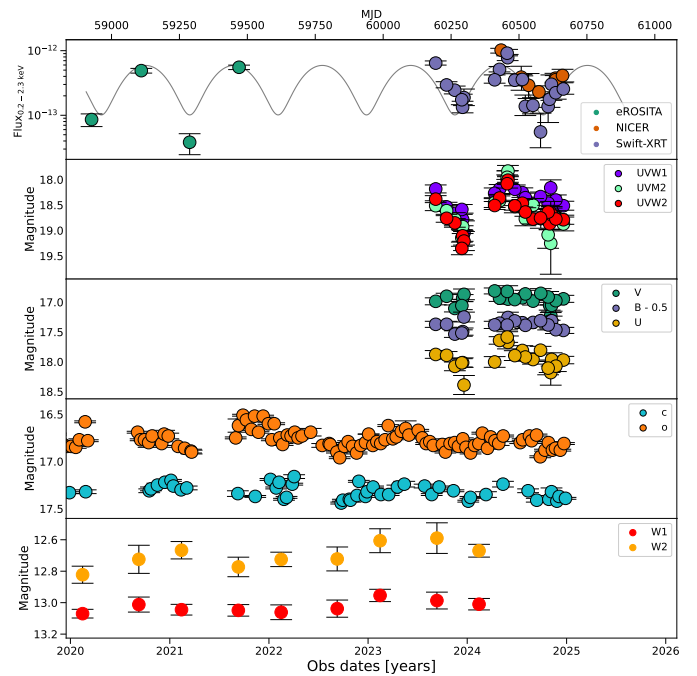
There is a 4-year window between the tentative start of the TDE and the lack of detection on the *Swift-XRT* monitoring

observations where the source might have been detected in X-rays. This window matches the decay time seen in the ATLAS and WISE light curves. The X-ray variability on eRASSt J0344-3327 could be explained by a repeating partial tidal disruption event (pTDE), similar to the variability found in eRASSt J045650.3-203750 (Liu et al. 2023, 2024). The TDE and the later "down-up-down-up-down" variability on eRASSt J0344-3327 matches the scenario proposed by Shu et al. (2020) where several flux dips occurred during the decay phase. The variability in Shu et al. (2020) is associated with X-ray flares from the stellar tidal disruption by a SMBHB candidate. A more detailed discussion about TDEs and X-ray quasiperiodic events is presented in Sect. 6.2.

### A.2. eRASSt J0530-4125

eRASSt J0530-4125 ( $z = 0.076$ ) is one of the most variable and best-studied eROSITA-selected SMBHB candidates. Only a *ROSAT* all-sky survey upper flux limit at a level of  $< 3 \times 10^{-13}$  erg  $\text{s}^{-1}$   $\text{cm}^{-2}$  in the 0.2–2.0 keV band is found in archival X-ray data, consistent with the faint flux level of the source.

The optical analysis of the source shows that eRASSt J0530-4125 has a galaxy-like spectrum with weak broad and narrow emission lines. The broad emission lines found in the spectrum, in particular  $\text{H}\beta$ , are not significantly detected, leading to an uncertain single-epoch SMBH mass measurement of  $\log M_{\text{bh}}/M_{\odot} = 7.26 \pm 0.48$ . Based on the optical narrow emission lines, the gas in the host galaxy appears to be ionized by star-formation processes instead of AGN.



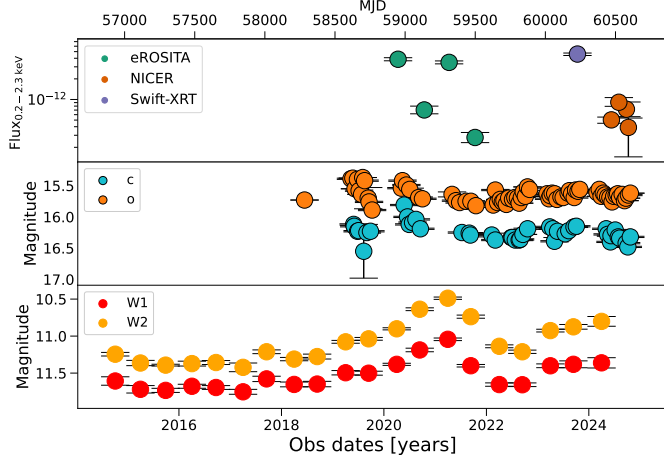
**Fig. A.2.** Multiwavelength light curve of eRASSt J0530-4125. The first panel shows the X-ray data from *SRG/eROSITA*+*Swift-XRT*+*NICER* at the 0.2–2.3 keV band. UV and optical light curves from *Swift-UVOT* are shown in the second and third panels, while optical and IR light curves, obtained from ATLAS and WISE, are displayed in the fourth and fifth panels, respectively.

Figure A.2 shows the multiwavelength data collected for eRASSt J0530-4125. We note that the UV bands of the *Swift-UVOT* light curves follow the variability trend defined by the

X-ray light curve. The hot and more energetic photons usually come from the vicinity of the SMBHs. Therefore, an X-ray-UV correlation is expected under the SMBHB scenario. ATLAS data provides a preliminary assessment of the host-galaxy contribution by subtracting a reference image from every observation. We do not notice any significant optical variability in this new (AGN-only) ATLAS light curve.

### A.3. eRASSt J1906-4850

eRASSt J1906-4850 (also known as LEDA 3904185) is a nearby ( $z = 0.049$ ) and luminous ( $L_{0.2-2.3 \text{ keV}} = (1.73 - 23.8) \times 10^{42} \text{ erg s}^{-1}$ ) Seyfert I galaxy with a double-peaked broad Balmer line in the optical spectrum, as shown in Fig. 5. One of the broad components is consistent in kinematics with the narrow Balmer line while the other component is redshifted by  $\Delta v = 2900 \pm 740 \text{ km s}^{-1}$ . According to the narrow line diagnostic diagram and the spectral shape of the optical spectrum, the source is consistent with being an AGN.



**Fig. A.3.** Multiwavelength observations of eRASSt J1906-4850.

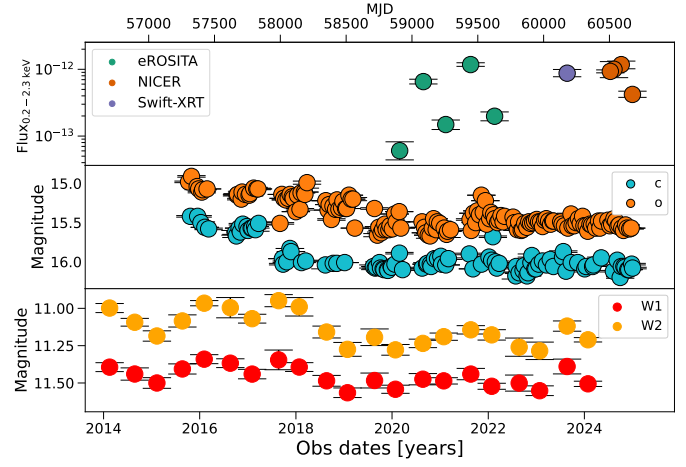
Two single-epoch SMBH masses were derived by assuming that each hypothetical SMBH is surrounded by an independent BLR, leading to rather low-mass measurements. The mass estimations based on the second and redshifted component of  $H\beta$  and  $H\alpha$  lines are  $\log(M_{\text{bh}}/M_{\odot}) = 6.64 \pm 0.38$  and  $\log(M_{\text{bh}}/M_{\odot}) = 7.50 \pm 0.23$ , respectively. Double-peaked broad Balmer lines have been proposed to indicate the presence of SMBHBs (see, e.g., Doan et al. 2020; Terwel & Jonker 2022). However, a disk-like BLR on a single SMBH can also reproduce double-peaked profiles tracing the gas located in the outer edge of the accretion disk and the inner edge of the BLR (Eracleous & Halpern 1994; Eracleous et al. 2009; Storchi-Bergmann et al. 2017).

Figure A.3 shows the X-ray, optical, and IR light curves of the galaxy eRASSt J1906-4850. Similar to eRASSt J0344-3327, the optical and IR light curves seem to have a pronounced peak before and during the SRG/eROSITA observations. However, the rise in brightness in the IR light curve takes longer than in eRASSt J0344-3327, making a TDE scenario less likely. The IR seems to lag the optical emission by two years, according to the peaks of the corresponding light curves. The multiwavelength landscape seems to match the behavior presented in eRASSt J0344-3327, where the X-ray "up-down" emission corresponds with the flux dimming after an increase in the brightness in optical and IR. However, the TDE scenario is disfavored based on the slow rise of the IR emission and the lack of features in the opti-

cal data. eRASSt J1906-4850 was detected by the *ROSAT* all-sky survey in September 1990 with a flux of  $\sim 3 \times 10^{-12} \text{ erg s}^{-1} \text{ cm}^{-2}$  in the 0.2–2.0 keV band, consistent with the faint flux levels of eRASSt J1906-4850.

### A.4. eRASSt J0432-3023

eRASSt J0432-3023 (ESO 421-9) is a Seyfert 2 Galaxy at a redshift of  $z = 0.055$ . It has been lately monitored by *NICER*, but further X-ray observations are needed to confirm or rule out the hint of periodic variability that this source presents. The multiwavelength light curve in Fig. A.4 shows no noticeable correlation between the X-ray, optical, and IR.



**Fig. A.4.** Multiwavelength observations of eRASSt J0432-3023. The data is similar to the data of Fig. A.1. The X-ray panel also displays *NICER* data shown with orange markers.

### A.5. eRASSt J1130-0806

eRASSt J1130-0806 (MCG-01-29-027:  $z = 0.037$ ) shows a galaxy-like spectrum with faint emission lines and the absence of broad Balmer lines. The optical counterpart of the SRG/eROSITA coordinates corresponds to a face-on spiral galaxy. The multiwavelength data (Fig. A.5) show optical variability. However, there is no correlation between the eROSITA and the optical data. The low luminosity X-ray data and the slightly large separation between the X-ray and optical coordinates could indicate the presence of off-nuclear sources, such as hyper-luminous objects (HLXs). For a discussion about non-nuclear objects that produce variable X-ray emission, see Sect. 6.2.

### A.6. eRASSt J1522-3722

eRASSt J1522-3722 was observed under our *NICER* program (#5141) to test its X-ray variability under the SMBHB scenario. The *NICER* monitoring program shows an X-ray dimming in the light curve, followed by an increase in the flux. However, our monitoring programs have been unable to catch the source in its faint flux state. The optical ATLAS data in Fig. A.6 seems to follow the pattern established by the X-ray data, especially between eRASS1 and eRASS2 and during the *NICER* monitoring program of early 2023.

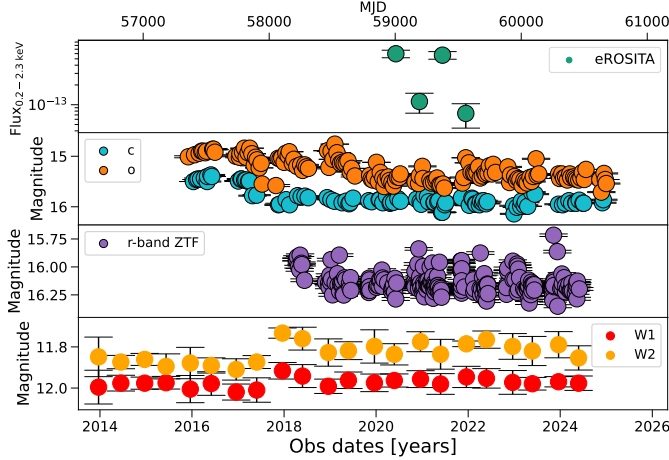


**Fig. A.5.** Multiwavelength observations of eRASSt J1130-0806. The data is similar to the data of Fig. A.1 with additional ZTF r-band data in the third panel.

eRASSt J1522-3722 (or 2MASS J15221541-3722488) is classified as an AGN candidate by the Strasbourg Astronomical Data Center (CDS-SIMBAD). Our newly obtained SAAO spectrum of eRASSt J1522-3722 shows broad Balmer emission lines, confirming the AGN nature of the source and a redshift of  $z = 0.064$ . The  $[\text{O III}]\lambda 5007\text{\AA}$  line was fitted with one narrow and one broad Gaussian line, indicating the presence of outflows. The galaxy falls into the HII region of the BPT because the  $[\text{O III}]$  line possesses multiple components, and only the narrow line was used for the diagnostic diagram.

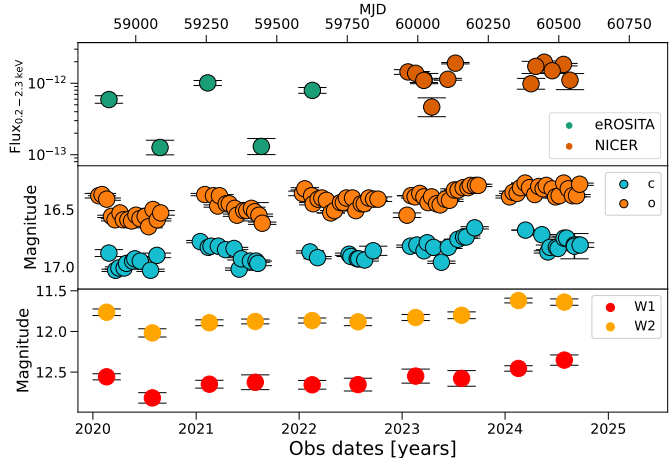


**Fig. A.6.** Multiwavelength observations of eRASSt J1522-3722. The data is similar to the data of Fig. A.4.

#### A.7. eRASSt J1141+0635

eRASSt J1141+0635 (or 2MASS J11415445+0635096;  $z = 0.101$ ) is one of the most monitored sources in our sample. Initially, the X-ray data visually suggested a periodic behavior with a tentative period of  $T \sim 120$  days. However, the source does not show any hint of periodic variability anymore. Lately, the *Swift*-XRT monitoring program showed a more ordered variability than in the previous observations. We emphasize that more X-ray observations are needed to disentangle the nature of this

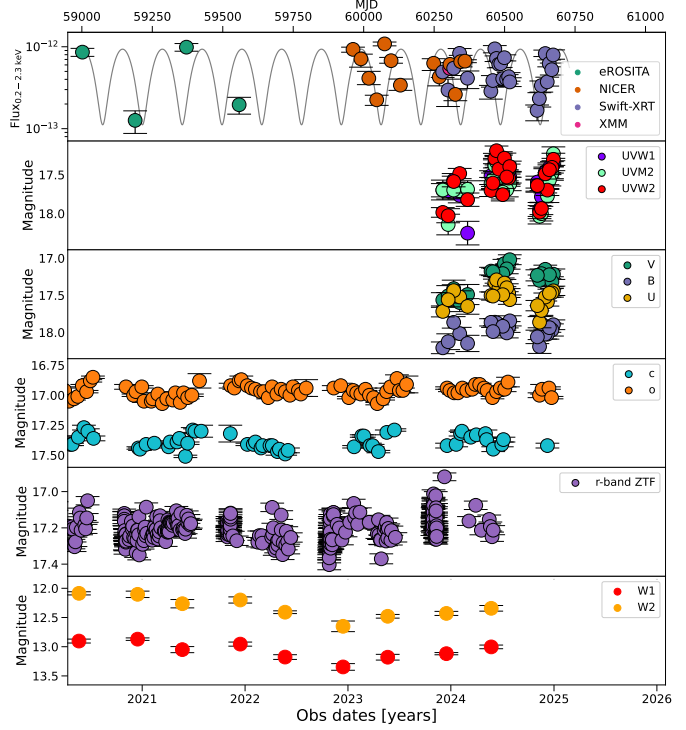


**Fig. A.7.** Multiwavelength observations of eRASSt J1141+0635. Similar to Fig. A.2 with additional ZTF data in the fifth panel.

source. We note that only the UV data follow the X-ray variability (Fig. A.7).

#### A.8. eRASSt J0458-2159

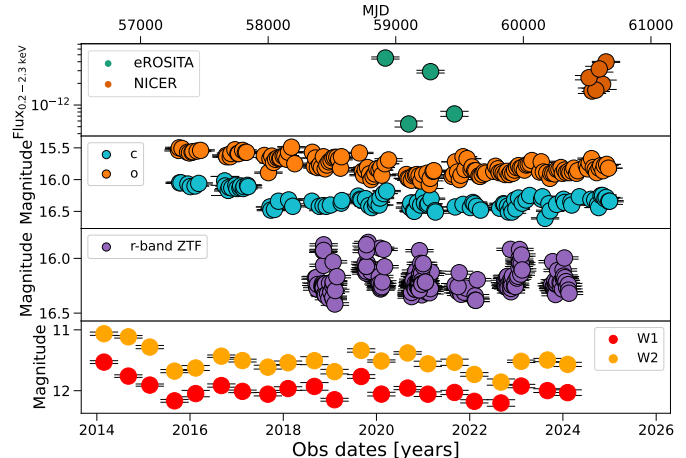


**Fig. A.8.** Multiwavelength observations of eRASSt J0458-2159. The data and markers are similar to those in Fig. A.2 with additional r-band ZTF optical data.

eRASSt J0458-2159 (ESO 552-39;  $z = 0.040$ ) is a Seyfert 1 Galaxy monitored by *NICER*. The source was observed with the *ROSAT* all-sky survey, *ROSAT*-PSPC, and *ROSAT*-HRI pointed observations with fluxes of 9.1, 2.0, and  $19.80 \times 10^{-13} \text{ erg s}^{-1} \text{ cm}^{-2}$ , respectively. The *ROSAT* data are consistent with the faint flux level of the source shown in Fig. A.8. The galaxy shows strong broad Balmer lines and

$[\text{O III}]\lambda 5007\text{\AA}$  emission line consistent with AGN emission, as shown by the BPT diagnostic diagram.

#### A.9. eRASSt J2227-4333

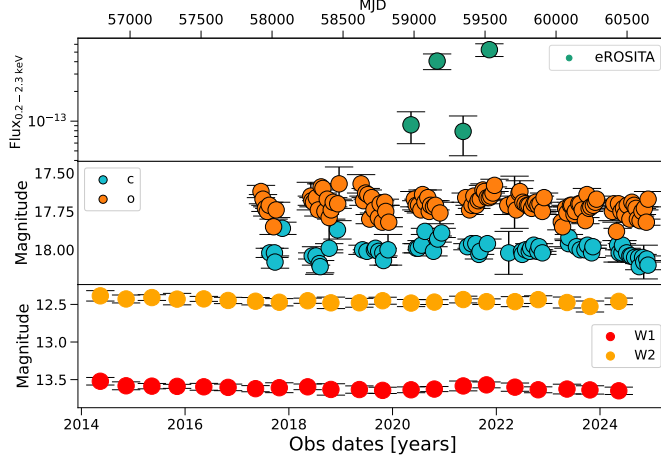


**Fig. A.9.** Multiwavelength observations of eRASSt J2227-4333. Data shown are similar to those of Fig. A.1.

eRASSt J2227-4333 (6dFGS gJ222755.8-433339) is a galaxy at redshift  $z = 0.198$  with a strong  $[\text{O III}]\lambda 5007\text{\AA}$  emission line but without very prominent broad Balmer lines, indicating a type II AGN. The optical and IR light curves of the source (Fig. A.9) are rather constant, and there is no clear relation with the eROSITA data.

#### A.10. eRASSt J1124-0348

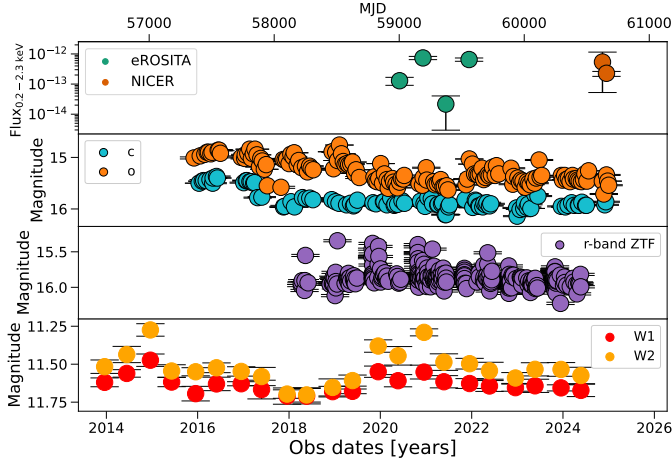


**Fig. A.10.** Multiwavelength observations of eRASSt J1124-0348. Data and markers similar as in Fig. A.5.

eRASSt J1124-0348 (or 6dFGS gJ112456.3-034840) is a low luminosity Seyfert II Galaxy with a redshift of  $z = 0.021$ . It only has a *ROSAT* all-sky survey upper limit of  $\sim 4 \times 10^{-13} \text{ erg s}^{-1} \text{ cm}^{-2}$  on the 0.2–2.0 keV band, consistent with the faint flux state of the eROSITA data. The optical spectrum reveals a galaxy-like spectral shape with a strong  $[\text{O III}]$  emis-

sion line relative to the  $\text{H}\beta$  line. The single-epoch SMBH can only be constrained using the slightly broad component of  $\text{H}\alpha$ .

The multiwavelength data in Fig. A.10 show interesting optical variability that apparently matches the IR peaks of 2021. It seems that these peaks in optical and IR are related to the X-ray variability. However, more data is needed to understand the nature of these features.

#### A.11. eRASSt J0036-3125

eRASSt J0036-3125 (LEDA 172477) is a galaxy at  $z = 0.108$  with weak emission lines and weak AGN features in the optical spectrum. Despite this, eRASSt J0036-3125 shows a luminous bright state in its X-ray light curve, reaching a luminosity of  $1.5 \times 10^{43} \text{ erg s}^{-1}$  in the 0.2–2.3 keV band.

The optical and IR emission appears to be lagging an increase in the X-ray emission traced by the eROSITA data (Fig. A.11). Additional X-ray data are needed to understand if the X-ray emission reaches a stable level again, similar to the optical and IR light curves.

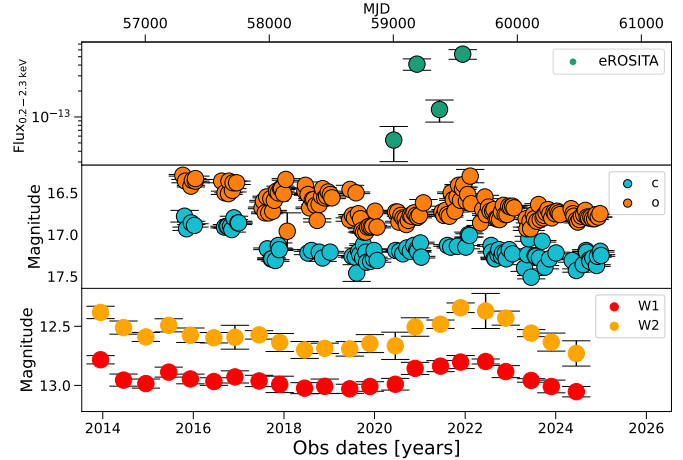


**Fig. A.11.** Multiwavelength observations of eRASSt J0036-3125. Data and markers similar as in Fig. A.1.

#### A.12. eRASSt J1003-2607

eRASSt J1003-2607 (RX J1003.2-2607) was classified as AGN by Kahabka et al. (2000) while studying the gas content of the dwarf galaxy NGC 3109 using *ROSAT* PSPC observations of background X-ray sources. No obvious extragalactic counterparts are detected at the X-ray position of the AGN, suggesting a very faint or distant object. Only a point source with a magnitude of  $m_r = 22.28$  is found within a radius of  $1.62''$  from the X-ray position in the LS DR10 images. The X-ray and UV light curve is shown in Fig. A.12.

Figure A.13 shows the LBT spectrum of the likely optical counterpart of eRASSt J1003-2607 and the spectrum extracted at an offset position. We extracted a spectrum of an off-source position to assess whether the observed emission lines are from the interstellar medium of the foreground galaxy or not. The source spectrum exhibits only two strong emission lines consistent with  $\text{H}\beta$  and  $\text{H}\alpha$  lines at the redshift of NGC 3109 ( $z = 0.0013$ ). The spectral analysis revealed that the Balmer emission lines are intrinsic to the targeted object and are not coming from the ionized gas of NGC 3109. This implies that the source has indeed an

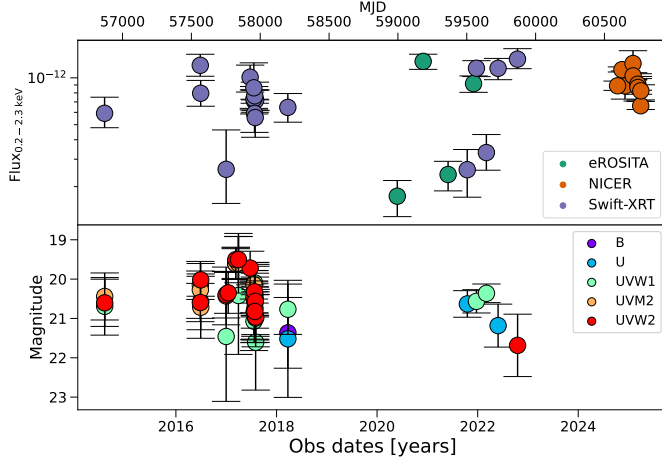


**Fig. A.12.** Multiwavelength observations of eRASSt J1003-2607. Only *Swift*-XRT (purple markers in top panel) and *Swift*-UVOT (bottom panel) observations in different bands were previously available for this object, covering almost 10 years of data. Additional *NICER* observations (orange markers) were obtained to monitor the X-ray evolution of the source.

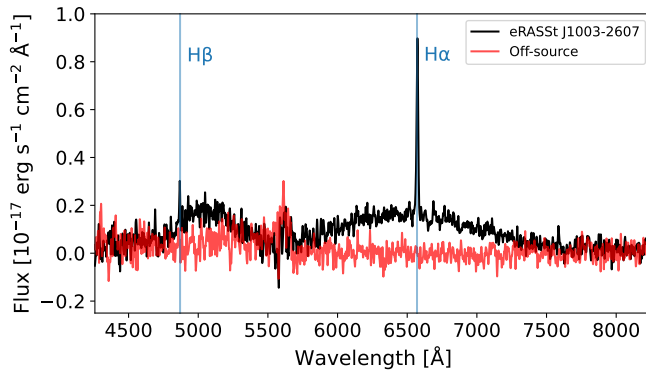


**Fig. A.13.** LBT optical spectrum of the tentative eRASSt J1003-2607 counterpart (black) and an off-source position (red). The source shows two emission lines consistent with being H $\beta$  and H $\alpha$  lines at a redshift of  $z = 0.001345$ . The lack of emission lines in the off-source position indicates that the lines belong to the tentative eRASSt J1003-2607 counterpart. The source is likely to be an HLX.

extragalactic nature. However, the object would have a distance consistent with NGC 3109 and an off-nuclear origin. Using the redshift of NGC 3109 as the redshift of the object, we derive a luminosity of  $\sim 4 \times 10^{39}$  erg s<sup>-1</sup> in the 0.2–2.3 keV band, likely corresponding to a ULX-like object. The source is, therefore, discarded as a SMBHB candidate. We note that there is a possibility that the targeted source is not the real counterpart of the X-ray emission. However, the FoV surrounding eRASSt J1003-2607 is very crowded, and according to Fig. 3, there is only one evident optical counterpart at the position of the X-ray source. Other scenarios, such as an optically faint AGN in the background, are plausible but very unlikely.

### A.13. eRASSt J0818-2252

eRASSt J0818-2252 (LEDA 80921,  $z = 0.034$ ) is a Seyfert I galaxy with strong AGN features such as broad Balmer lines and strong [O III] lines. The X-ray from Fig. 8 and Fig. A.14

seems to follow a quasiperiodic behavior with timescales of  $\sim 300$  days. More X-ray monitoring programs are needed to confirm periodicity in eRASSt J0818-2252. The IR and optical brightness increased by  $\sim 0.5$  mag in 2016 and 2019, respectively. The source was detected by the *ROSAT* all-sky survey and later by a pointed *ROSAT* HRI observation with fluxes of  $\sim 3 \times 10^{-12}$  erg s<sup>-1</sup> cm<sup>-2</sup> and  $\sim 4 \times 10^{-13}$  erg s<sup>-1</sup> cm<sup>-2</sup>, respectively. Both *ROSAT* observations are consistent with the bright and faint eROSITA flux levels.

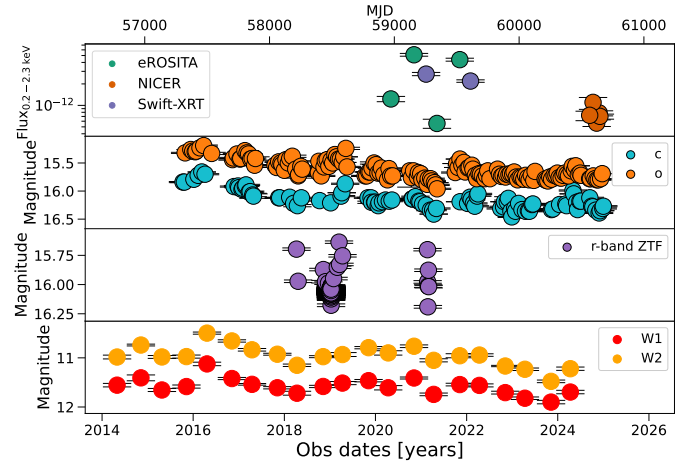


**Fig. A.14.** Multiwavelength observations of eRASSt J0818-2252. The data is similar to the data of Fig. A.1 with additional ZTF r-band data in the third panel. The X-ray panel also displays NICER data with orange markers.

### A.14. eRASSt J0600-2939

eRASSt J0600-2939 is a galaxy at  $z = 0.104$  with an optical spectrum that shows weak H $\beta$ +[O III] emission lines. Only the broad H $\alpha$  line was used to estimate a single-epoch SMBH mass measurement. No clear trends are found in the multiwavelength light curve (Fig. A.15).

### A.15. eRASSt J0044-3313

eRASSt J0044-3313 shows evidence of AGN emission according to its broad Balmer lines and BPT classification. Similarly to eRASSt J1906-4850, the spectral profile of the broad H $\alpha$  component looks asymmetric and can be modeled by two broad Gaussian lines. This feature is only seen in H $\alpha$ . A single broad component can model the H $\beta$  line due to the noise and low SNR in the blue part of the spectrum. The velocity shift between both components is  $\Delta v = 1800 \pm 500$  km s<sup>-1</sup>. Using the second H $\alpha$  component, we derive a SMBH mass of  $\log(M_{\text{bh}}/M_{\odot}) = 7.63 \pm 0.45$ , which is consistent with the H $\beta$  measurement. The ATLAS data in Fig. A.16 shows an increase in the optical light curve that is temporally consistent with the X-ray data from eROSITA. The source was detected in X-ray by the *ROSAT* all-sky survey with a flux of  $\sim 4.5 \times 10^{-13}$  erg s<sup>-1</sup> cm<sup>-2</sup> on the 0.2–2.0 keV band.

### A.16. eRASSt J0614-3835

eRASSt J0614-3835 shows a Seyfert II optical spectrum hosted by a galaxy at  $z = 0.054$ . The source was detected in X-ray by the *ROSAT* all-sky survey with a flux of  $\sim 4 \times 10^{-13}$  erg s<sup>-1</sup> cm<sup>-2</sup>

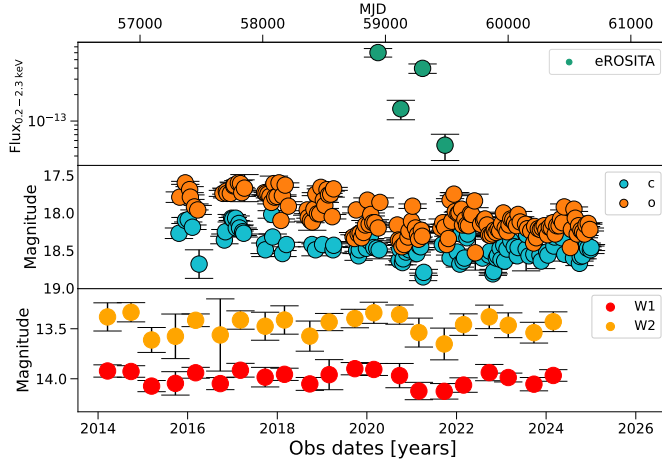


**Fig. A.15.** Multiwavelength observations of eRASS J0600-2939. The data is similar to the data of Fig. A.1.

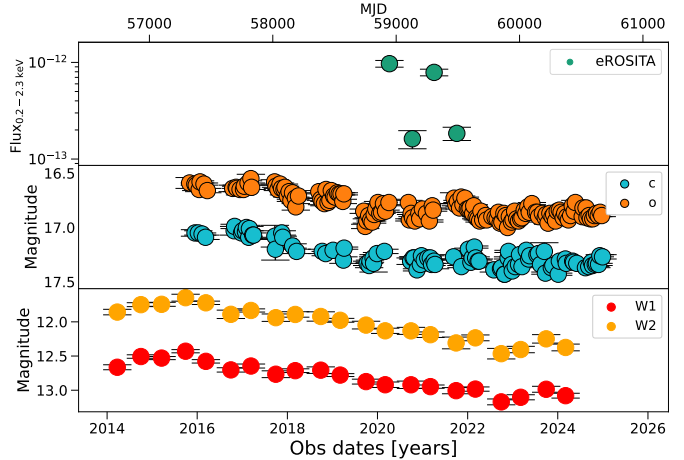


**Fig. A.17.** Multiwavelength observations of eRASS J0614-3835. The data is similar to the data of Fig. A.1.

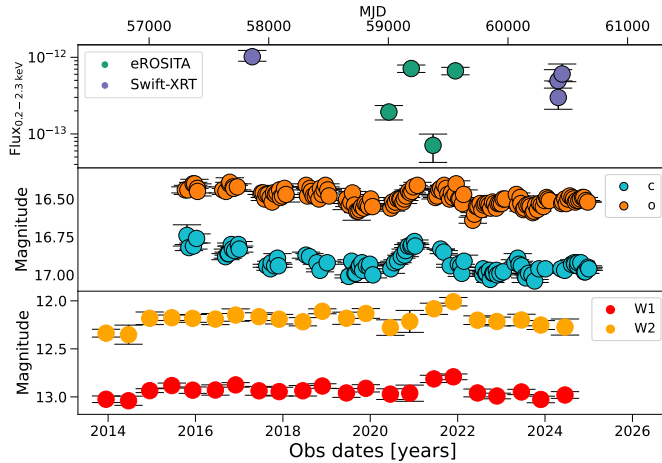


**Fig. A.16.** Multiwavelength observations of eRASS J0044-3313. The data is similar to the data of Fig. A.1.

on the 0.2–2.0 keV band, between the bright and faint eROSITA flux levels of Fig. A.17.